REVIEW ARTICLE

Aided- and self-assembly of the liquid crystalline nanoparticles in bulk and in solution: computer simulation studies

A. Slyusarchuk[a], D. Yaremchuk[b], J. Lintuovori[c], M. R. Wilson[d], M. Grenzer[e], S. Sokołowski[f] and J. Ilnytskyi[b]

[a] Institute of Enterprise and Advanced Technologies of the Lviv Polytechnic National University, 79044, Lviv, Ukraine;
[b] Institute for Condensed Matter Physics of National Academy of Sciences of Ukraine, 79011, Lviv, Ukraine;
[c] Univ. Bordeaux, CNRS, LOMA, UMR 5798, F-33400 Talence, France;
[d] Department of Chemistry, Durham University, University Science Laboratories, Lower Mountjoy, Stockton Road, Durham, DH1 3LE, UK;
[e] Leibniz Institute of Polymer Research, 01069 Dresden, Germany;
[f] Department of Theoretical Chemistry, Faculty of Chemistry, Maria Curie Skłodowska University, 20031 Lublin, Poland

ARTICLE HISTORY
Compiled December 24, 2022

ABSTRACT

We review computer simulation studies of aided and self-assembly of nanoparticles that are decorated with liquid crystalline (mesogenic) ligands, termed hereafter as liquid crystalline nanoparticles (LCNPs). In bulk, LCNPs self-assemble into ordered morphologies, typically displaying a polydomain structure. We demonstrate that a range of monodomain morphologies can be grown by changing the density of ligands and employing external fields of specific symmetry which act on mesogens. It is also demonstrated that the speed of self-assembly of LCNPs with chromophoric (e.g. azobenzene) mesogens can be increased by applying illumination at a certain wavelength and polarization. Another case study covers the formation of an interconnected macromolecular network in a solution of the LCNPs in a polar solvent. Here, the network structure depends strongly on the decoration pattern of the LCNPs. Finally, the adsorption of LCNPs on a compatible liquid crystalline brush is discussed with a focus on the prerequisites and optimal conditions for this phenomenon. The review demonstrates the ability of classical particle-based models to produce a molecular-based understanding of the structure and interactions of LCNPs, and also to reproduce a wide set of physicochemical phenomena related to LCNP aided- and self-assembly processes.

KEYWORDS
self-assembly; liquid crystalline nanoparticles; molecular dynamics; azobenene

1. Introduction

Nanoparticles attract much attention because of their unique optical, electronic, magnetic and chemical properties [1]. A number of their practical applications are known

---

CONTACT J. Ilnytskyi. Email: iln@icmp.lviv.ua

already in areas such as medical diagnostics, drug delivery, cancer therapy, nanoelectronics and information storage, sensors, (photo)catalysis and surface coatings [2]. As it is pointed out in Ref. [3], the main focus can be narrowed down to such aspects as: "(i) the synthesis of functionalized nanoparticles; (ii) their phase behavior when mixed with a homopolymer matrix and their assembly into well-defined superstructures; (iii) the role of processing on the structures realized by these hybrid materials and the role of the mobilities of the different constituents; (iv) the role of external fields (electric, magnetic) in the active assembly of nanoparticles; and (v) the engineering properties that result and the factors that control them".

Self-assembly of nanoparticles lies at the centre of a field of advanced materials development termed "nanoarchitectonics" [4]. This process can be made more controllable by modification (decoration) of nanoparticles with specific functional ligands. A good example of such a system, are nanoparticles that have been functionalised by liquid crystalline (LC) ligands [5–10], particles that have been termed LCNPs.

The structure of the self-assembled morphology is defined by the type of the core nanoparticle (metal/non-metal, magnetic/non-magnetic, etc.); grafting density, length, flexibility and chemical details of ligands; number and type of functionalisation groups and decoration pattern [5–10]. The prerequisite for self-assembly to occur is the presence of external conditions, such as temperature, pressure/density, properties of a solvent, presence of surfaces or reaction to an external field. The prediction of the symmetry/structure/properties of self-assembled morphologies, that depend on all these factors, is immensely challenging.

Computer simulations are of great importance in tackling this challenge. Simulation models that incorporate the relevant details of complex molecular architectures and tackle the statistical behaviour of many-particle systems under varying external conditions, can provide a "molecular level" picture of aided and self-assembly processes. In particular, they provide the means of understanding how these processes can be controlled under differing external conditions. Modelling at this level is highly demanding, as the models must span a wide range of time- and length scales that are typically required for supramolecular self-assembly. For example, if full chemical-specific details are taken into account, then only small system sizes and short simulation times can be studied. However, a good compromise can be achieved by using elements of a multiscale approach [11,12], which builds a coarse-grained model based on the simulation data of a more chemically-detailed model. Such a coarse-grained model is of rather generic type, capturing essential physical details of the atomistic system, and allowing simulation of the required time- and length scale to see self-assembly [13,14]. Due to the inevitable loss of specific chemical details, the comparison with particular chemical realisations is performed on a high level only, via the symmetry and the structure of observed morphologies, their reaction in response to external fields, and via the temperature- or density-driven phase transitions between morphologies of different type.

This paper collects the results for aided- and self-assembly of LCNPs of various molecular architectures, by means of coarse-grained molecular dynamics simulations. These are the results of intensive collaboration between Ukrainian researchers and their partners in the UK, Germany and Poland. Sec. 2 contains modelling and simulation details for typical coarse-grained models capable of studying aided- and self-assembly in LCNPs. In Sec. 3 we consider the temperature-related effects of the self-assembly. Sec. 4 covers the role played by the decoration pattern of LCNPs in the assembly process. In Sec. 5 we describe the photo-aided self-assembly of LCNPs containing azobenzene chromophores. Sec. 6 contains results on the formation of macromolecular networks in LCNPs solution that are dependent on the decoration patterns of the LCNPs. Sec. 7 covers the study of LCNP adsorption on a LC polymer brush. Findings are summarized in the Conclusions section.

2. Coarse-grained modelling

All results presented in this study are obtained employing a coarse-grained modelling approach where the relevant groups of atoms are treated as single beads that interact with one another via soft-core potentials. The model LCNP is shown schematically in the top left frame of Fig. 1. It is built from a spherical central core and N_{ch} ligands that are bonded to the center of a core but otherwise are free to move on its surface. Each ligand is terminated by a mesogen. The model may also be used to represent a generation three carbosilane dendrimer, where the internal degrees of freedom of a dendritic scaffold allow sufficient conformation flexibility that the orientations of the mesogens are not severely restricted by the details of the scaffold structure [15,16]. In the later case, the model is motivated by the original work of Ponomarenko *et al.* [17] who characterised the thermal behavior of the carbosilane LC dendrimers (see Fig. 1) by means of polarizing optical microscopy, differential scanning calorimetry, and X-ray diffraction. The use of different generation dendrimers (as shown in Fig. 1) provides a means of changing the grafting density around a central core. These are just part of various families of liquid crystalline dendrimers, which, in addition to carbosilanes [18,19], includes polyorganosiloxanes [20], poly(propyleneimines) [21] and poly(amidoamines) [22].

In total, four different types of beads are involved: a large core sphere representing the nanoparticle, two sizes of smaller spherical spacer beads, and a spherocylinder mesogen. If a solvent is present, it is represented by spherical beads of the same size as the smaller spacer bead. Dimensions of all beads can be found in Tab. 1.

Interaction potentials are chosen to mimic features of each group of atoms that are represented either by a soft sphere or a soft spherocylinder. Each pair $\{i, j\}$ of the interacting particles is characterized by a set of variables, $\mathbf{q}_{ij} = \{\widehat{\mathbf{e}}_i, \widehat{\mathbf{e}}_j, \mathbf{r}_{ij}\}$, where $\widehat{\mathbf{e}}_i$ and $\widehat{\mathbf{e}}_j$ are the unit vectors that define the orientation of the respective particles in space, whereas $\mathbf{r}_{ij}$ is the vector that connects their centers of mass. For the case of spherical particles, their orientations are not defined. The closest distance, $d(\mathbf{q}_{ij})$, between two interacting particles is defined according to the top right image in Fig. 1. Then, the scaling factor σ_{ij} is evaluated for the pair, where $\sigma_{ij} = (\sigma_i + \sigma_j)/2$ for two spherical particles, $\sigma_{ij} = D$ for two spherocylinder particles, and $\sigma_{ij} = (\sigma_i + D)/2$ for the mixed pair. The dimensionless closest distance between two interacting particles is defined as $d'(\mathbf{q}_{ij}) = d(\mathbf{q}_{ij})/\sigma_{ij}$.

Using these notations, the general form of the pair interaction potential between ith and jth beads, that is of the soft attractive (SAP) type, can be written in a compact dimensionless form

$$V^{\mathrm{SAP}}[d'(\mathbf{q}_{ij})] = \begin{cases} U\big\{[1 - d'(\mathbf{q}_{ij})]^2 - \epsilon'(\mathbf{q}_{ij})\big\}, & 0 \le d'(\mathbf{q}_{ij}) < 1 \\ U\big\{[1 - d'(\mathbf{q}_{ij})]^2 - \epsilon'(\mathbf{q}_{ij}) \\ \qquad - \frac{1}{4\epsilon'(\mathbf{q}_{ij})}[1 - d'(\mathbf{q}_{ij})]^4\big\}, & 1 \le d'(\mathbf{q}_{ij}) \le d'_c \\ 0, & d'(\mathbf{q}_{ij}) > d'_c \end{cases} \tag{1}$$

Table 1. Force field parameters, derived originally in Ref. [15] and extended for the case of LCNPs

parameter	description	value
σ_1	core diameter	$21.37\,\text{Å}$
σ_2	first spacer bead diameter	$6.23\,\text{Å}$
σ_3	the rest spacer beads diameter	$4.59\,\text{Å}$
σ_s	solvent beads diameter	$4.59\,\text{Å}$
D	mesogen cap diameter	$3.74\,\text{Å}$
L/D	mesogen aspect ratio	3
U (regular)	repulsion strength	$70 \cdot 10^{-20}\text{J}$
U (strong)	repulsion strength	$140 \cdot 10^{-20}\text{J}$
U'_a	attractive energy parameter	21.43
ϵ'_1	attractive energy parameter	1.714
ϵ'_2	attractive energy parameter	-1.714
m_1	core mass	$62.44 \cdot 10^{-25}\text{kg}$
m_2	first spacer bead mass	$2.20 \cdot 10^{-25}\text{kg}$
m_3	the rest spacer beads mass	$0.70 \cdot 10^{-25}\text{kg}$
m_s	solvent beads mass	$0.70 \cdot 10^{-25}\text{kg}$
m	mesogen mass	$3.94 \cdot 10^{-25}\text{kg}$
I	mesogen moment of inertia	$6.00 \cdot 10^{-24}\text{kg}$
l_1	bond length: core – first spacer bead	$14.9\,\text{Å}$
l_2	bond length: first – second spacer bead	$3.60\,\text{Å}$
l_3	bond length: rest spacer bonds	$3.62\,\text{Å}$
l_4	bond length: last spacer bead – mesogen	$2.98\,\text{Å}$
k_b	bond spring constant	$50 \cdot 10^{-20}\text{J}/\,\text{Å}^2$
θ_1	pseudo-valent angle for linear fragments	π
θ_2	pseudo-valent angle at branching points	$\pi/2$
k_a (fully flexible)	pseudo-valent angle spring constant	0
k_a (semi-flexible)	pseudo-valent angle spring constant	$20 \cdot 10^{-20}\text{J}/rad^2$

where U defines repulsion strength. The dimensionless well depth of this potential

$$\epsilon'(\mathbf{q}_{ij}) = \left\{ 4\Big[U'_a - 5\epsilon'_1 P_2(\widehat{\mathbf{e}}_i \cdot \widehat{\mathbf{e}}_j) - 5\epsilon'_2 \Big(P_2(\widehat{\mathbf{r}}_{ij} \cdot \widehat{\mathbf{e}}_i) + P_2(\widehat{\mathbf{r}}_{ij} \cdot \widehat{\mathbf{e}}_j)\Big)\Big] \right\}^{-1}, \tag{2}$$

is obtained from the condition, that both the expression (1) and its first derivative on $d'(\mathbf{q}_{ij})$ turn to zero when $d'(\mathbf{q}_{ij}) = d'_c$, where $d'_c = 1 + \sqrt{2\epsilon'(\mathbf{q}_{ij})}$ is the cutoff separation of the potential [23]. $\widehat{\mathbf{r}}_{ij} = \mathbf{r}_{ij}/r_{ij}$ is a unit vector connecting the centers of two beads, U'_a, ϵ'_1 and ϵ'_2 are dimensionless parameters that define the shape of the interaction potential. Therse are chosen to represent the "model A" in Ref. [23], all three values are listed in Tab. 1. $P_2(x) = (3x^2 - 1)/2$ is the second Legendre polynomial.

The effective well depth, $\epsilon'(\mathbf{q}_{ij})$, influences both the shape of the attractive part and, via d'_c, its range. When the parameters, contained in the expression for $\epsilon'(\mathbf{q}_{ij})$, are such, that it asymptotically reaches zero, the cutoff d'_c approaches 1 and the interval for the second line in Eq. (1) shrinks to zero. As a result, in this limit, one retrieves the soft repulsive potential (SRP) of a quadratic form

$$V^{\text{SRP}}[d'(\mathbf{q}_{ij})] = \begin{cases} U\,[1 - d'(\mathbf{q}_{ij})]^2, & 0 \le d'(\mathbf{q}_{ij}) \le 1 \\ 0, & d'(\mathbf{q}_{ij}) > 1 \end{cases}, \tag{3}$$

that is used typically in the dissipative particle dynamics simulations [24]. This limit is illustrated in Fig. 2 by the blue curve and is marked as $\epsilon'(\mathbf{q}_{ij}) \to 0$.

The expression for the bonded interactions written for a single LCNP has the following form:

$$V_b = \sum_{i=1}^{N_b} k_b(l_i - l_0)^2 + \sum_{i=1}^{N_a} k_a(\theta_i - \theta_0)^2, \tag{4}$$

where N_b and N_a are the total numbers of bonds and pseudovalent angles in a single molecule, l_0 and θ_0 are respective reference values for each of these harmonic terms. Pseudovalent angles introduce semiflexibility for linear fragments of chains and orthogonality for the side chains, if present, see Fig. 3 (a) and (b), respectively. For fully flexible chains we set $k_a = 0$. Terminal attachment of a mesogen is managed by the bond between the center of its spherical cap and the last particle of a spacer, see the same figure (c), whereas a lateral attachment is performed between respective centers of these particles, see the same figure (d). Required orientation of a mesogen with respect to the spacer is controlled in both cases by the pseaudovalent angle that involves the center of a mesogen, see (c) and (d). For this specific pseudovalent angle the value $k_a > 0$ is always used. Alternatively, the orientation of a mesogen can be controlled by introducing instead a special angular term [25,26]. All parameters involved in bonded interactions are listed in Tab. 1.

The behaviour of these models can be studied using coarse-grained molecular dynamics. Here, the simulations can be carried out with the GBMOLDD [27,28] program extended to the case of the $NP_xP_yP_zT$ ensemble [29] and to the case of coarse-grained soft-core potentials. A single Nóse-Hoover thermostat has been used in most cases for both translational and rotational degrees of freedom. In quenching or rapid heating runs velocity rescaling was used instead. The timestep $\Delta t \sim 20\,\mathrm{fs}$ (typically $10 - 20\times$ larger than possible within fully atomistic models) was used for velocity rescaling runs, whereas a smaller timestep of $\Delta t \sim 10 - 15\,\mathrm{fs}$ was required for the runs using the thermostat. Because of mostly repulsive pair interactions between the majority of beads, the external pressure of $50 - 70$ atm is applied via three barostats, one for each spatial axis [29], which ensures an average density of about $0.7\,\mathrm{g/cm}^3$ (i.e. close to that expected in experimental systems composed of organic mesogenic ligands).

3. Self- and field-aided assembly of terminally decorated LCNP in a melt

Molecular dynamics simulations of the aided and self-assembly of 100 LCNP in a melt state were performed in Ref. [30]. In addition to the link with liquid crystalline dendrimers (as discussed in section 2), we note the link here with liquid crystalline functionalised gold [6] and silver nanoparticles [31] and their interest as potential metamaterials. In such systems, the gold or silver particle provides the central scaffold, leading to materials whose properties are potentially tunable through systematic variation of nanoparticle size, flexibility of linking groups, and variation in mesogenic shape, chirality and functionality.

The coarse-grained model discussed in Sec. 1 contained $N_{\mathrm{ch}} = 8-64$ side chains with terminal attachment of mesogens (mesogen is collinear to the bond that links it to the spacer). The case of $N_{\mathrm{ch}} = 32$ was covered in more detail in Ref. [16]. The aim of these simulations was twofold. An initial target is to reproduce the experimentally observed sequence of lamellar smectic, hexagonal discotic and cubic morphologies [6,17,32–38] when the decoration density, given by N_{ch}, progressively increases. The LCNP was expected to adopt the rod-like, disc-like and spherulitic shape in these respective cases, providing the means of the relation between the molecular shape and morphology of the melt [6,17]. Secondly, the possibility of self-assembly within the melt into both mono- and poly-domain morphologies was examined.

Because of the strong correlation between the LCNPs shape and the morphology symmetry [6,16,17], the analysis can be focused on the changes in the LCNP conformations, expecting the symmetry of ordered morphology to follow these. Conformational analysis starts from the evaluation of the components of the gyration tensor for each k-th LCNP:

$$G^{[k]}_{\alpha\beta} = \frac{1}{N^{[k]}} \sum_{i=1}^{N^{[k]}} (r^{[k]}_{i,\alpha} - R^{[k]}_{\alpha})(r^{[k]}_{i,\beta} - R^{[k]}_{\beta}), \quad \vec{R}^{[k]} = \frac{1}{N^{[k]}} \sum_{i=1}^{N^{[k]}} \vec{r^{[k]}_i}, \tag{5}$$

where $N^{[k]}$ particle centers with coordinates $r^{[k]}_{i,\alpha}$ are taken into account, $R^{[k]}_{\alpha}$ is the molecular center of mass, α, β denote Cartesian axes. Each mesogen is replaced by a line of four centers. The eigenvalues of the gyration tensor, $\lambda^{[k]}_1 > \lambda^{[k]}_2 > \lambda^{[k]}_3$, provide the molecular "roddicity" (always positive)

$$a^{[k]}_r = [\lambda^{[k]}_1 - \frac{1}{2}(\lambda^{[k]}_2 + \lambda^{[k]}_3)][R^{[k]}_g]^{-2} \tag{6}$$

and "discoticity" (always negative)

$$a^{[k]}_d = [\lambda^{[k]}_3 - \frac{1}{2}(\lambda^{[k]}_2 + \lambda^{[k]}_1)][R^{[k]}_g]^{-2}, \tag{7}$$

that are evaluated for each kth LCNP. Here, $[R^{[k]}_g]^2$ is the squared radius of gyration. The LCNP is classified as a rod with asphericity $a' = a^{[k]}_r$ if $|a^{[k]}_r| > |a^{[k]}_d|$, and it is classified as a disc with the asphericity $a' = a^{[k]}_d$ otherwise. As a result, the system is split into the rods and discs subsystems, with their fractions f_r and f_d, respectively.

Spontaneous self-assembly of the melt of LCNP with $N_{\mathrm{ch}} < 64$ ligands results in the formation of a mixture of rod- and disc-like shapes, see snapshots in Fig. 4. The former prevail at $N_{\mathrm{ch}} < 24$, whereas the latter predominates at $N_{\mathrm{ch}} > 24$. Histograms showing the distribution of molecular asphericity are given in the left frame of Fig. 5. At $N_{\mathrm{ch}} \geq 64$ both histograms merge indicating, in this case, a shape close to a spherical one, $a' \to 0$. Typical molecular conformations are shown in Fig. 5, right frame. Respective fractions of the rod- and disc-like LCNP conformations within a melt of LCNPs are shown in the middle frame of the same figure. One, hence, observes a conformational bistability of the LCNPs with $24 < N_{\mathrm{ch}} < 64$ ligands.

As was shown in Ref. [16], the rod-like and disk-like molecular conformations of LCNPs are evidenced via the uniaxial and equatorial planar arrangements of their ligands. This leads to the intriging idea that rod-like and disk-like conformations can be induced by reorienting the terminal mesogens by external field of a suitable symmetry. Both uniaxial and planar fields can be introduced via an additional energy term

$$U_{\mathrm{rot}} = -F(\mathbf{e}_i \cdot \mathbf{i})^2, \tag{8}$$

where the field amplitude $F > 0$ represents a uniaxial case and $F < 0$ a planar one,

$\mathbf{e}_i$ is the orientation of the ith mesogen and $\mathbf{i}$ defines the field direction. Magnetic or electric fields can be seen as the physical realisation of an uniaxial field, whereas the planar arrangement of mesogens can be achieved either for the mesogens with a transverse dipole moment, or as the result of cyclic photoisomerization of azobenzene chromophoric mesogens [39]. In this way, one expects to break conformational symmetry and promote formation of a monodomain morphology commensurable with the symmetry of the external field. After field-aided simulation, the resulting morphology is then equilibrated at a required temperature with the field switched off.

Respective snapshots for the lamellar smectic A ($\mathrm{Sm_A}$), columnar and cubic phases are shown in Fig. 6. Application of appropriate symmetry fields leads to an essential redistribution of molecular conformations during the field-assisted assembly of LCNPs, as is shown in Fig. 7. Disc-like conformations, however, are not dominant for small number of ligands, $N_{\mathrm{ch}} < 22$, as in this case the number of chains is insufficient to form a disc-like shell of ligands. These estimates are, of course, model dependent and a surface density of ligands will be a more universal measure for the rod-to-disc conformation transition. Hence, both packing abilities and imposed orientations of the mesogens play a role in the field-assisted assembly of LCNPs with variable number of ligands. Detailed analysis of the structure of all morphologies for the case of $N_{\mathrm{ch}} = 32$ ligands was performed in Ref. [16].

One can conclude this section by saying that the suggested coarse-grained model for the LCNPs captures the main features of real experimental systems by reproducing a set of morphologies that take place at specific grafting densities of ligands. These systems, like their experimental counterparts, are prone to metastability effects, but formation of a monodomain morphology can be promoted by an external filed with the required spatial symmetry.

4. Field-aided assembly of laterally decorated LCNP in a melt

Ordered morphologies of LCNPs belong to a class of the so-called meta- or functional materials, where mechanical and electro-optical properties both play a significant role in potential applications. Such morphologies can be interpreted as molecular networks, where LCNP cores play the role of vertices and the ligands form physical bonds – i.e. the links. In this interpretation, the anisotropy of mechanical response will be chiefly determined by the spatial arrangement of the LCNP cores, whereas the electro-optic properties will depend on arrangement of mesogens and, in some cases, by the cores as well (as in the case of surface plasmomic resonance for metal nanoparticles).

In Sec. 3 we covered the case of a terminal attachment of the ligand mesogens (Fig. 1), and the LCNPs of such molecular architecture were found to self-assemble into the $\mathrm{Sm_A}$ and Col morphologies [16,40]. The former morphology is lamellar, where the layers can be characterized by a layer normal $\mathbf{a}$. It is also optically uniaxial, characterised by the nematic director $\mathbf{n}$ collinear to $\mathbf{a}$ (see leftmost frame in Fig. 6). On the other hand, the Col morphology is a supramolecular assembly of columns, where each column is composed of a stack of disc-shape LCNPs. The arrangement of columns is uniaxial and can also be described via a vector $\mathbf{a}$. However, there is no global nematic order of mesogens in this case, as their orientations are distributed radially, see Fig. 5, right frame. Therefore, the optical response of the Col morphology is essentially different from that of the $\mathrm{Sm_A}$ one, bearing some analogy to the difference in opto-mechanical applications of the main- and side-chain LC architectures, see e.g. Ref. [41].

It is clear from Figs. 1 and 6, that the radial orientation of mesogens in a Col phase is the result of the energy penalty associated with bending of the ligand spacer. Lateral attachment of the LC bead, see, the left frame of Fig. 8, is also possible from the viewpoint of chemical synthesis [32], and may open up a possibility of greater orientation freedom of mesogens. In particular, one may expect the presence of an optically uniaxial columnar morphology, as shown in the right frame of Fig. 8.

To study such possibility, the coarse-grained model of LCNPs discussed above was modified in Ref. [40] to mimic lateral arrangement of mesogens with respect to the spacer, following study [42], where such simulations were performed at a semi-atomistic level. This type of attachment is depicted in Fig. 3 (d) and discussed therein.

Only one case with $N_{\mathrm{ch}} = 32$ ligands was considered and the assembly of LCNPs with laterally attached mesogens was field-assisted. The field was directed along the OZ axis and its magnitude in Eq. (8) was set equal to $F = 2 - 4 \cdot 10^{-20}$J. The system was held under the range of pressures of $P = 50 - 200\,\mathrm{atm}$. For all values of the pressure the system indeed assembled into the uniaxial hexagonal columnar morphology depicted schematically in Fig. 8 (right frame) and referred thereafter as uCol$_h$. This morphology was used as an initial state and then a series of subsequent runs were performed at a selected set of temperatures with the field switched off, aimed at examinating the temperature stability of this phase.

For the analysis of the structural changes undergone by the system upon changing the temperature, a number of order parameters were considered. The level of orientational order of mesogens was described by the nematic order parameter:

$$S_N = \langle P_2(\mathbf{e}_i \cdot \mathbf{n}) \rangle_{i,t}\,, \tag{9}$$

where $\mathbf{e}_i$ characterizes the orientation of the ith mesogen, $\mathbf{n}$ defines the nematic director axis, and $P_2(x) = \frac{1}{2}(3x^2 - 1)$ is the second Legendre polynomial. The averaging is performed over all mesogens in a system and over the time trajectory denoted as $\langle \ldots \rangle_{i,t}$. We also introduce the hexagonal order parameter S_H within the XY plane, and the columnar order parameter S_C defined as follows

$$S_H = \left\langle \left| \frac{1}{N_k} \sum_{k=1}^{N_k} e^{6j\varphi_i} \right| \right\rangle_{i,t}\,, \quad S_C = \left\langle \frac{N_{c,i}}{N_{\max}} \right\rangle_{i,t}\,. \tag{10}$$

Here φ_k is the polar angle of the bond between kth and selected central ith LCNPs, where the summation is performed over all kth LCNPs that belong to a first coordination sphere of ith LCNP (see, Fig. 9 (a)), $j = \sqrt{-1}$. $N_{c,i}$ is the number of LCNPs such that their centers are found inside the cylinder of $R_c = 1\,\mathrm{nm}$ drawn around the core of the ith LCNP orientated along the Z axis (see, Fig. 9 (b)), and $N_{\max}$ is the normalisation factor introduced for the sake of convenience.

Changes in the values of all order parameters, S_N, S_H and S_C, upon the temperature rising are shown in Fig. 9, right frame. At low temperatures, $T < 400K$, all three order parameters are essentially non-zero indicating the uniaxial hexagonal columnar phase uCol$_h$, characterized by uniaxial nematic order, high columnarity, and high hexagonal order of the columns. The vector characterizing the columns, $\mathbf{a}$, is now collinear with the nematic director $\mathbf{n}$, similar to the case of the Sm$_{\mathrm{A}}$ phase discussed above. With the increase of the temperature beyond 400 K, all order parameters gradually decay, but while S_N decays very fast, almost linearly, the decay of S_H and S_C with the rise in temperature is slower. As a result, there is a narrow temperature range around $T =$

450 K, where the value of S_N dropped to about 0.1 (typical for the isotropic phase), but S_H and S_C are still almost the same as in the case of the uCol$_h$ morphology at $T = 300-400$ K. This corresponds to the morphology, wCol$_h$, with a weak hexagonal order but disordered mesogens. It has the properties of an isotropic phase. The transition from uCol$_h$ to wCol$_h$ is gradual and the boundary between both, as shown in Fig. 9, is rather approximate. Heating the system beyond 480 K results in the drop for both order parameters, S_H and S_C, to their minima indicating a completely disordered morphology [40].

To summarize this section, the simulations of the melt of the LCNPs with lateral attachment of mesogens reveal the presence of two novel discotic morphologies with a non-zero hexagonal order parameter S_H. One, uCol$_h$, is characterised by an uniaxial nematic order of mesogens, whereas another, wCol$_h$, by disordered mesogens. These results support initial expectations for the existence of the optically uniaxial discotic phase, as sketched in the right frame of Fig. 8. Snapshots for both morphologies can be found elsewhere [40].

5. Photo-aided assembly of the chromophore-containing LCNP in a melt

As commonly seen experimentally, cooling a disordered melt of model LCNPs leads to self-assembly into a polydomain structure, with individual domains exhibiting partial orientational order. This scenario was found in simulation studies in Refs. [16] and [30] and was illustrated above in Fig. 4. A more thorough analysis of self-assembly in such systems is provided in Ref. [43], in the context of photocontrollable self-assembly of azobenzene-functionalized nanoparticles. The findings of these studies are discussed below.

We note in passing, that control of functionalized nanoparticles using light provides rich areas of study, where order, aggregation and material properties are potentially all tunable by light radiation [44]. Synthetically, chromophoric functional groups (such as azobenzene, cinnamoyl, diarylethene dithiophenols, etc.) can all be grafted onto a nanoparticle. Applications so far have included photocontrolled liposomes [45] and micelles [46], optically switchable devices [46] and networks of functional nanoparticles with optically switchable conductance [47].

The case of a melt of 200 LCNPs, each containing $N_{\rm ch} = 12$ terminally attached ligands, was considered. From the histograms shown in Fig. 5, disc-like conformations of the LCNPs with $8 \leq N_{\rm ch} \leq 16$ are suppressed. This inhibits the formation of columns. A perfect monodomain Sm$_{\rm A}$ phase was obtained first by application of an uniaxial field (8). It was equilibrated then at various temperatures $T = 400 - 520K$ with the field switched off.

We focused on molecular asphericity defined as

$$A = \left\langle \frac{3}{2}\,\frac{\sum_{\alpha=1}^{3}[\lambda_\alpha^{[k]}]^2}{\left[\sum_{\alpha=1}^{3}\lambda_\alpha^{[k]}\right]^2} - \frac{1}{2} \right\rangle_{k,t}, \tag{11}$$

where $\lambda_\alpha^{[k]}$ is the set of eigenvalues of the gyration tensor of the kth LCNP, defined in Eq. (5), and the averaging is performed over all LCNPs and a time trajectory.

The LCNPs in the Sm$_{\rm A}$ phase have distinctively rod-like conformations (see Fig. 5), therefore it is instructive to monitor their orientational and positional order. In doing that, each k-th LCNP is treated on the level of its equivalent ellipsoid, and its orientation $\mathbf{E}_k$ is defined by the eigenvector that corresponds to the largest eigenvalue $\lambda_1^{[k]}$ of the gyration tensor. Then, the nematic order parameter, S_2, for the LCNPs is evaluated according to the equation

$$S_2 = \langle P_2(\mathbf{E}_k \cdot \mathbf{N}) \rangle_{k,t}\,, \tag{12}$$

where $\mathbf{N}$ stays for the nematic director evaluated for an ensemble of LCNP orientations $\{\mathbf{E}_k\}$.

Finally, smectic order in a system of LCNPs provides a level of "lamellarity" in the arrangement of LCNPs. It is quantified via the amplitude of the density wave for the coordinates $\mathbf{R}_k$ for the centres of the LCNPs cores along the layer normal. For the case of the $\mathrm{Sm_A}$ phase, the latter is assumed to be collinear with $\widehat{\mathbf{N}}$. The smectic order parameter is evaluated then by founding the maximum of the expression

$$S(p) = \max \left| \langle e^{j2\pi(\mathbf{R}_k \cdot \widehat{\mathbf{N}})/p} \rangle \right|_{k,t}\,, \tag{13}$$

as a function of p. The maximum position $p_{||}$ provides the pitch of the $\mathrm{Sm_A}$ phase, whereas the smectic order parameter is defined as $S_s = S(p_{||})$.

The clusters (domains) of the $\mathrm{Sm_A}$ phase are identified, based on the mutual positions of adjacent LCNPs, and their number N_{clust} and the size of the largest cluster, M_{clust}, are evaluated. For the sake of convenience, both are normalized by the number of LCNPs in the system, N, resulting in the reduced number of clusters $N_c = N_{\text{clust}}/N$ and the normalized maximum cluster size $M_c = M_{\text{clust}}/N$. More technical details are provided in Ref. [43].

The changes in values of A, S_2, S_s, N_c and M_c upon heating of a monodomain $\mathrm{Sm_A}$ sample are shown in Fig. 10. We note that a separate run was performed at each temperature, shown in these plots, starting from a monodomain $\mathrm{Sm_A}$ sample each time. All of them change sharply at $T^* \approx 510\,\mathrm{K}$. Specifically, at $T < T^*$, LCNPs adopt essentially a non-spherical shape ($A \approx 0.6$) with high values for both order parameters, S_2 and S_s. At $T > T^*$, LCNPs turn into a spherical shape ($A \to 0$) with both order parameters approaching zero. The transition at $T = T^*$ is then the $\mathrm{Sm_A}$ to isotropic one. The behaviour of the reduced number of clusters N_c and the maximum cluster size M_c reveals three types of cluster structure. In the $\mathrm{Sm_A}$ phase ($T = 400 - 500\,\mathrm{K}$) one has $N_c \to 0$ and $M_c \to 1$, i.e. a single cluster containing all 200 LCNPs. The system is found in the monodomain $\mathrm{Sm_A}$ phase. On the opposite side, in the I phase ($T > 520\,\mathrm{K}$), $N_c \to 1$ and $M_c \to 0$ indicating no $\mathrm{Sm_A}$ clusters (200 disjoint LCNPs). The transition region, $T = 500 - 520\,\mathrm{K}$, is characterised by a sharp decrease of the maximum cluster size and sharp increase of the number of clusters.

The reverse transition, spontaneous self-assembly of the monodomain $\mathrm{Sm_A}$ morphology upon cooling down the high-temperature isotropic phase, is found to be strongly dependent on the cooling rate. It can be achieved at a cooling rate of $0.37K/\,\mathrm{ns}$, whereas at a cooling rate higher than $0.75K/\,\mathrm{ns}$, the melt is trapped in a metastable polydomain state (for more details, see Ref. [43]).

Further analysis indicated strong dependence of the dynamical properties of LCNPs on temperature. In particular, the melt was quenched at each temperature of interest for 30 ns and the initial $1-8\,\mathrm{ns}$ of each run were analysed (the first 1 ns were skipped to allow the temperature to stabilise itself). The initial $1-8\,\mathrm{ns}$ were split into time blocks at time instances $\{t_k\}$ of equal duration $\delta t = t_k - t_{k-1} = 0.2\,\mathrm{ns}$. The instantaneous translational and rotational diffusivities of LCNPs were introduced as

$$d(t_k) = \frac{1}{6\,\delta t}\Big\langle\big[\mathbf{R}(t_k) - \mathbf{R}(t_{k-1})\big]^2\Big\rangle, \tag{14}$$

$$r(t_k) = \frac{1}{2\,\delta t}\Big\langle\big[\widehat{\mathbf{E}}(t_k) \cdot \widehat{\mathbf{E}}(t_{k-1})\big]^2\Big\rangle \tag{15}$$

averaged over all LCNPs and evaluated at each t_k. Their time-averages over initial $1-8$ ns are related to short-time translational $D = \langle d(t_k)\rangle$ and rotational $R = \langle r(t_k)\rangle$ diffusion coefficients of the LCNPs at the early stage of the self-assembly. Their temperature dependence is shown in Fig. 11 (middle and right frames, black symbols marked as "no illum") and one observes essentially higher values of both in the vicinity of 500 K, whereas at lower temperatures, both D and R decrease sharply indicating a slowing down of both translational and rotational mobility of LCNPs.

The reason for the restricted mobility of LCNPs must be attributed to strengthening the chromophore-chromophores LC interaction. It manifests itself in: (i) formation of $\mathrm{Sm_A}$ domains, and (ii) establishing the inter-domain physical crosslinks, see snapshots in Ref. [43]. However, while the effect (i) acts towards the self-assembly of a monodomain $\mathrm{Sm_A}$ phase, the effect (ii) works against this goal by preventing the rearrangement of individual domains. As a result, at lower temperatures one observes physically cross-linked domains, similarly to the case of side-chain LC polymers [48,49].

To quantify the orientational arrest of chromophores at lower temperatures, their rotation relaxation time has been estimated as a function of temperature [43]. This was done based on the assumption that the orientation time autocorrelation function $\langle\widehat{\mathbf{e}}(t) \cdot \widehat{\mathbf{e}}(0)\rangle$ decays exponentially with time [50,51]

$$C(t) = \big\langle\widehat{\mathbf{e}}(t) \cdot \widehat{\mathbf{e}}(0)\big\rangle \sim \exp\big[-\frac{t}{t_{\mathrm{rot}}}\big], \tag{16}$$

where t_{rot} is defined as the rotation relaxation time. The evaluation time interval is restricted again to the initial $1-8$ ns of each run. The dependence of t_{rot} on temperature shows an essential increase of $1-1.5$ order of magnitude upon lowering the temperature from 500 K down to 350 K, see Fig. 11 (right frame, black legends marked as "no illum").

Photo-aided self-assembly of a monodomain $\mathrm{Sm_A}$ morphology is based on the following considerations. In general, illumination will affect the azobenzene-containing system by: (A) weakening (or eliminating) the LC order, and/or (B) promoting an order-order transition [52]. (A) is based on the dilution of the LC phase, formed by *trans*-isomers, by non-mesogenic *cis*-isomers. It may decrease the LC order or even initiate a so-called photochemical phase transition [52–55]. (B) is the result of the angularly selective photoisomerization of *trans*-isomers which results in their gradual reorientation perpendicularly to the light polarization axis [56,57]. If the light propagation vector is collinear to the Z-axis and the beam itself is unpolarised, the *trans*-isomers will stay predominantly collinear to the Z-axis, in which case they are always perpendicular to the light polarization axis [52]. More details on the choice of the parameters leading to realistic modelling of photo-induced reorientation of azobenzene are provided elsewhere [39,43].

Therefore, if both (A) and (B) are applied in a controlled way, they both could aid self-assembly of a monodomain morphology. Indeed, the dilution of *trans*-isomers by nonmesogenic *cis*-isomers can weaken the inter-domains links (the main obstacle for the self-assembly at lower temperatures) and promote higher diffusion of the LCNPs.

Then, the $\mathrm{Sm_A}$ domains are expected to reorient themselves following reorientation of *trans*-isomers of each LCNP collinearly to the Z-axis. This is confirmed by the computer simulations undertaken in Ref. [43].

The presence of illumination has been found to have a profound effect on the chromophores rotation relaxation time t_{rot}, as evidenced in the left frame of Fig. 11 (red legends marked via "illum"). Specifically, t_{rot} reaches a plateau at the temperatures $T < 400K$ and it is lower than in the case of no illumination with a factor of 2.5 at 350 K. This indicates an essential speed-up of the chromophores' reorientation dynamics under illumination. The same effect of faster dynamics is observed also for the translational and rotational diffusion of LCNPs, shown in the middle and right frames of the same figure. Note the essential difference between the no illumination and illuminated cases in the temperature range of $460 - 500\,\mathrm{K}$. As the result, as has been found in Ref. [43], illumination indeed essentially speeds-up the self-assembly of azobenzene-containing LCNPs. The cooling runs, performed under illumination, indicated that the temperature dependence for the set of characteristics, A, S_2, S_s, N_c, and M_c, is comparable with the set obtained with no illumination applied, but now at the cooling rates of about $3 - 4$ higher.

To confirm the effect of illumination, a set of runs was performed, where the system was rapidly quenched (by the instance change of simulation temperature) from the isotropic state with the presence of illumination. The results, obtained for A, S_2, S_s, N_c, and M_c, are shown in Fig. 12. These can be compared now with their counterparts in Fig. 10, which were obtained by heating up the perfectly ordered monodomain initial sample. One finds curves of similar respective shapes in both cases, save for the shift of the curves in the photo-assisted assembly to somewhat lower temperatures. The latter might be explained by the hysteresis effect.

As is demonstrated by this simulation study, photo-aided self-assembly is based on a weakening of the chromophore-chromophore interaction. The effect is small inside individual domains that have been already reoriented, as far as the chromophores are oriented mostly perpendicular to the polarization vector there, and are rarely photoisomerised. On the contrary, frequent photoisomerizations occur for isotropically oriented chromophore-chromophore inter-domain links. Such selectivity leads to intelligent steering of the system towards the monodomain phase. The practical outcomes of the photocontrollable self-assembly are: (i) the possibility to apply up to $2 - 5$ times higher cooling rates, when self-assembly is performed starting from the high-temperature isotropic state, and (ii) the possibility to form a monodomain ordered phase at low temperature, starting directly from a glass-like state.

6. Macromolecular networks of LCNP with various decoration patterns in solution

So far, in Secs. 3-5 the model LCNPs were considered, in which the ligands are free to diffuse on the surface of a spherical core, which makes sense in several cases. One example is the LC dendrimer, where the spherical core mimics the internal dendritic scaffold and, therefore, the ligands may rearrange and appear at different positions on the effective boundary of such a scaffold at each given time instance. Another example is the nanoparticle, decorated via uncontrolled random process, and diffusion of ligands on its surface in a course of simulations ensures that averaging is performed over many possible realizations of ligands positions. Using the analogy with magnetic systems, one can term such decoration approach as an "annealed" system. However, in the case of some organic or inorganic cores and ligands, it is possible to control the precise position of ligands on the core surface.

There is a range of particular spatial arrangements that are reported in experimental studies. These utilize segregation of ligands, selective decoration at crystal facets, edges, terraces, and vertices [58–63], as well as the use of specific cores, e.g. discotic ones, with well-defined flat arrangement of ligands [64–66]. One can also expect that further novel methods of synthesis of nanoparticles possessing patchy ligand shells with a specific pre-designed patterns will be developed in the future. In general, the type of spatial pattern of the LCNPs is expected to affect greatly the symmetry of the resulting self-assembled morphology. The possibility to control the type of final morphology by imposing certain pre-designed decoration patterns on the LCNP surface, stimulated computer simulation of such systems, as performed in Ref. [67].

The pattern types shown in Fig. 13, are motivated by existing experimental reports mentioned above, whereas the rest should be treated as theoretical generalizations. The patterns are utilized by applying additional constraints onto the ligands, as suggested in Refs. [14,68]. More specifically, one builds the scaffold of grafted beads, each bonded to the center of the core sphere, and on top of that, their mutual spatial arrangement is defined by a set of additional bond and angle interactions. As a result, the scaffold may rotate on the surface of a central core, but only as a single entity, keeping the mutual arrangement of its patchy bunches fixed throughout the simulation. The soft spherical core allows a variety of possible chemical realizations: metal nanoparticle, dendritic or another hyper-branched scaffold, discotic conjugated aromatic core and others (see Fig. 13). Each ligand is bonded to the center of a core unit via its first bead, followed by a spacer and the terminal mesogen. The number of ligands $N_\mathrm{l} = 12$ is kept the same in all patterns.

The ROD pattern has $1D$ patching symmetry with two patches located at the polar regions of the core unit, each formed of 6 ligands (left most panel in Fig. 13). The evidence for the experimental realization of such a pattern can be found in Refs. [62,69]. The TRI pattern has been reported in [69]. Another possibility for the experimental realization of both TRI and QTR patterns, is provided by the discotic core of conjugated aromatic rings, as shown in Refs. [64,66]. Both TRI and QTR models have $2D$ patching symmetry, and their natural continuation is the EQU model with twelve single ligand patches arranged equidistantly on the equator of the core unit. This patching pattern is a part of the decorated nanoparticles reported in Ref. [62] and may possibly be realized using discotic core units shown in Fig. 3 of Ref. [66]. Finally, the models AXI and HDG have $3D$ patching symmetry. In the former, six patches of 2 ligands each are arranged along each of three axes and the interpatch angles are introduced similarly to the case of the QTR model. In the HDG model, there are twelve single ligand patches arranged uniformly on the surface of the core unit, namely, on the vertices of a regular icosahedron resulting in a hedgehog-like appearance. The closest experimental realisations are, possibly, those based on tetrahedral decorations of the fullerene pseudo-spherical polyhedra [70,71].

We will discuss the simulation setup briefly here, and further specific details can be found in Ref. [43]. Both bottom and top walls of a simulation box are decorated by a monolayer of spherical particles of the same dimension as the core units of LCNPs. Assuming all nanoparticle cores to be of a noble metal, e.g. gold, the core-core interaction potential of a special form is used, which mimicks the presence of the electric double layer around such core particles, for more details, see Ref. [67]. As before, mesogen-mesogen interactions are of the SAP type, see Eq. (1) and parameters therein. Other pairs interact via the SRP potential (3). In the initial state of each run, the box interior is filled by $N_{\rm mol} = 9 - 64$ LCNPs in a random way, the remaining volume is filled by a solvent. The total density is tuned to be approximately the same as that for the case of bulk melt of LCNPs discussed in Secs. 3-5.

The main mechanism for forming a macromolecular network is attractive LC-LC interactions between mesogens of adjacent LCNPs and, as a result, the formation of inter-molecular links. The formation of such links is additionally strengthened by the solvophobicity of the ligand chains. It is expected that the type of a macromolecular network is strongly dependent on the symmetry of a decoration pattern. For instance, the ROD pattern has dipole symmetry and is expected to form linear aggregates; the TRI, QTR and DSC patterns are best suited for formation of 2D sheets, whereas the AXI and HDG patterns are expected to form a 3D network structure.

Computer simulations were performed for each type of decoration pattern, depicted in Fig. 13, and in a wide range of concentrations given by the number of LCNPs $N_{\rm mol} = 8 - 64$. Five attempts of network formation were performed in each case and the results were averaged over them. The typical appearance of macromolecular networks is illustrated in Fig. 14 for the case of $N_{\rm mol} = 27$. In most cases, polydomain samples were observed, but the expected type of the network, as discussed above, was found indeed to dominate in each case. For instance, a clear 2D sheet can be seen in Fig. 14 for the DSC pattern, whereas highly interconnected 3D structures are found for the AXI and HDG pattern types.

Although the system is rather small to obey the statistical laws of networks [72], nonetheless, examining a range of related characteristics is instructive in clarifying some of its properties. First, we split the system into connected clusters, based on the set of existing intermolecular links, and then the size of the largest cluster, $S_{\rm max}$, and its span along the OZ axis, $Z_{\rm max}$, are evaluated [67]. Both properties are normalized and vary within a range from 0 to 1. Network connectivity is characterized by the average vortex rank K, the local clustering coefficient C, and the effective wall-to-wall spring constant, E. The latter is found by assuming each intermolecular link to acts as an elastic spring, followed by application of the Kirkhoff rules introduced for electric resistors [73]. For more details, see Ref. [67].

The time evolution of all these characteristics at a fixed number of the LCNP, $N_{\rm mol} = 27$, is shown in Fig. 15. The results were averaged over five runs. The dynamics of network formation is found to depend strongly on the decoration pattern. In particular, out of six patterns only three, AXI, DSC, and TRI, form single networks that percolate between the walls of a simulation box ($S_{\rm max}$ and $Z_{\rm max}$ both approach 1), with the QTR pattern being just short of achieving the same result. The remaining, ROD and HDG patterns are unable to form a single network (low $S_{\rm max}$ and $Z_{\rm max}$ values). The AXI LCNPs form a highly branched (high K) weakly clustered (low C) gel, while the DSC pattern forms almost the same highly branched but highly clustered (high C) network. Both of these happen on the time scale of up to 1 ns. The network of TRI LCNPs forms relatively slowly, on a time scale of about 5 ns and the resulting network is both weakly branched (low K) and with low values for the clustering coefficient C. The effective spring constant of the network with respect to the walls is the highest for the cases of AXI and TRI patterns, both are characterized by a low clustering coefficient C, but is low for the case of DSC pattern characterized by a high value for C. This has a simple intuitive explanation: at high clustering coefficient C most of the available links are used for connecting LCNPs with adjacent neighbours, whereas the remaining number of links is insufficient to provide strong interconnectivity between local clusters to ensure high value of an effective spring constant.

The analysis related to the potential application of such gels to catalysis is provided in Ref. [67]. In particular, network characteristics are examined in a broad interval of N_{mol} from 10 to 64, the limiting cases represent dilute solutions and bulk melt of LCNPs, respectively. The radial distribution functions and diffusion coefficients for the LCNPs cores are also studied. In short, the AXI decoration pattern is found the most robust one from the point of view of network formation dynamics and the robustness of its structure, as given by K, C and E values. The optimal density solution for application of such a gel for catalysis is also estimated. For these and more details, see Ref. [67].

To conclude this section, we ought to remark, that here we have a clear example of the use of computer simulations for predicting a collective behaviour of a statistical ensemble of particles with complex structure, in a situation where theoretical approaches cannot be applied with ease. This model system provides us with a useful sketch for the relation between the details of molecular architecture and the symmetry of the ordered structure such molecules assemble into. The results may have direct practical application to catalysis and related applications.

7. Interactions of LCNP with a (LC) polymer brush

One of the efficient ways to control the assembly of nanoparticles is by the use of functional or structured surfaces [74]. One example of this is a polymer brush [75,76]. Within the composite material containing both nanoparticles and a brush, several scenarios are possible: (i) nanoparticles and brush can phase separate; (ii) particles can be adsorbed on a surface of a brush and form a $2D$ structure there; (iii) particles may be localised within the brush and arranged into a $3D$ structure; for a more detailed review, see Ref. [77]. The fine details of the respective $2D$ or $3D$ structures depend on many factors such as brush composition and density, type of solvent, etc. In particular, for strong nanoparticle-polymer interactions, an ordered $2D$ array is only formed at a particular brush density, whereas at higher or lower density, the distribution of NPs demonstrate large spatial fluctuations and the packing order is reduced. For weak nanoparticle-polymer interactions, nanoparticles arrange into a hexagonal array on top of the polymer brush at high enough grafting density to result in a dense brush [77]. In the arrangement (ii), a brush of diblock copolymer may act as a functional material capable of moving nanoparticles on its surface [78], or nanoparticles may slide down to the valleys formed on a brush surface [79]. Transitions between the different arrangements are possible as well, e.g. the transition (iii) $\to$ (i) takes place in diblock copolymer brush that acts as a stimuli-sensitive and controllable release system for nanoparticles [80].

Adsorption of nanoparticles into a brush, arrangement (iii), leads to a composite material with a synergy of the properties of both constituents. As discussed in Ref. [81], a brush can function as a nanocomposite matrix acting as a reaction chamber for nanoparticles synthesis, a scaffold for immobilization of nanoparticles or as a capping agent for blocking the aggregation of nanoparticles, leading to new related applications. These are in the area of catalysis, sensors, new optical materials, nanoelectrodes, antimicrobial, antiadhesive, and nanomagnetic materials. For more details, see Ref. [81].

Most experimental, theoretical, and simulation works carried out in this field, consider undecorated nanoparticles but concentrate on different types of brushes, e.g. mixed brush, diblock-polymer brush, nanopatterned brush, etc. However, when both the nanoparticles and the brush contain similar LC groups, their interaction became more specific and spatially-resolved, as well as controllable by light if the LC groups are chromophoric, e.g. azobenzenes [82–86]. This opens up many possibilities for photo-controlled adsorption/desorption of such LCNPs by the LC polymer brush and related applications for controlled drug release, catalysis, and organic electronics developments. In this section, we cover the study of the adsorption of LCNPs on the LC polymer brush in terms of the system structure and dynamics by molecular dynamics computer simulations.

Such a system has been studied in Ref. [87], where the LCNPs with the HDG decoration pattern (see Fig. 13) was considered. As discussed in Sec. 6, the formation of a single network, in this case, is suppressed. This choice of the system is based on the need to promote possible adsorption of such LCNPs on the brush instead. The brush molecules are of the side-chain architecture containing a backbone of 36 beads and 12 side chains that are distributed uniformly across it. Each side-chain contains a two-bead spacer and a terminal mesogen of the same type as in the LCNPs. The first bead of each backbone is grafted to the bottom surface of the simulation box chosen as the $z = 0$ plane, as shown in Fig. 16.

The model system is contained within a simulation box with the dimensions $L_x = L_y = 21.8$ and $L_z = 54.5$ in reduced units, where a unit length is equal to the diameter of a spacer bead. Periodic boundary conditions are applied along OX and OY axes and elastic reflections occur when the bead crosses one of $z = 0$ or $z = L_z$ walls. $L_z = 54.5$ is chosen due to the requirement that the maximum extension of the brush molecules should not exceed $L_z/2$. A set of grafting densities of the brush is considered with, respectively $N_B = 0$, 1, 4, 9, 16, 25, and 36 brush molecules, with their ends grafted at the vertices of a square grid. The number of NPs is fixed at $N_{NP} = 20$. The rest of the simulation box is filled with the solvent until the total density of the solution reaches a value of 0.5 g cm^{-3}. The simulations are performed via molecular dynamics in the NVT ensemble at a temperature of $T = 480$ K.

For each number of brush molecules, N_B, five “adsorption” runs were performed, each of duration 20 ns. During the adsorption runs, the mesogens attract each other via potential (1) and form physical crosslinks. Because LC groups are present both in the LCNPs and in the brush, the aggregation of the LCNPs in the bulk part of the simulation box and their adsorption on the brush will compete. The result of the competition is expected to depend on the grafting density, i.e. the number N_B of brush molecules. Each such run is preceded by a “refreshing” equilibration run of the same duration, during which the attraction between the mesogens was switched “off”, i.e. the repulsive interaction potential given by equation (3) is used instead of the attractive one of equation (1). This leads the LCNPs to deaggregate and desorb from the brush and also allows them to diffuse throughout the simulation box. System properties in the adsorption regime are evaluated by averaging the data obtained during the last 4 ns of each adsorption run.

The normalized density profiles for the LCNP cores along the Z-axis,

$$n_{\mathrm{NP}}(z) = \frac{N_{\mathrm{NP}}(z)}{N_{\mathrm{NP}}}, \tag{17}$$

were evaluated, where $N_{\mathrm{NP}}(z)$ is the number of cores located at the distance z from the $z = 0$ wall. The histograms for $n_{\mathrm{NP}}(z)$ are stacked together in Fig. 16, right frame. With no brush molecules present, $N_B = 0$, one sees the layering of the LCNPs near each wall, with the peak heights gradually decaying and their widths increasing as one moves away from the walls ($20 < z < 35$). The density profile at $N_B = 4$ indicates no visible changes and minor changes in the middle of the box are seen at $N_B = 9$. At $N_B = 16$, the profile in the middle region of the box disappears, whereas the width of the second peak, as counted from the $z = 0$ wall, increases. This indicates adsorption of the LCNP from the middle region of the box into the upper part of the brush. With a further increase of N_B ($N_B = 25, 36$), two changes are observed: (i) $n_{\text{NP}}(z)$ becomes smeared in the brush region $z < 20$, and (ii) some LCNPs escape from the brush into the middle region of the box. This may indicate that the adsorption of LCNPs in this case is hindered by the high density of the brush and that expels the extra LCNPs.

The presence of an optimal value of $N_B \approx 16$ for the adsorption of NPs in a brush in this particular model is clearly seen through the evaluation of the cumulative number density of LCNPs

$$c_{\text{NP}}(z) = \sum_{z_i < z} n_{\text{NP}}(z_i), \tag{18}$$

which is a fraction of LCNPs cores separated from the bottom wall at the distance less than z (the analogue of the uniaxial coordination number). The plots for $c_{\text{NP}}(z)$, shown in Fig. 17, indicate at $N_B = 0, 4, 9$ a step-like dependence along z with five separate plateaus, each one emerging after a complete layer of NPs. At $N_B = 16$, the second and third plateau merge into a single large one, showing the adsorption of LCNPs into the brush at $z \approx 18$. With the increase of N_B up to 36, the steps for $c_{\text{NP}}(z)$ disappear for all $z < 30$ and are found again only in the bulk part of the simulation box, $z > 30$.

These changes in the LCNPs arrangement are visualised in a series of snapshots in Fig. 17. One observes a gradual increase of the effective brush height and straightening of the chains with the increase of N_B, typical for the regime of a denser brush. These two factors, and the increase in the number of mesogens within a brush, must be responsible for the enhanced adsorption of NPs at $N_B < 16$, peaking at $N_B \approx 16$. With the further increase of N_B, two other factors dominate: a lack of an accessible volume for NPs within a brush and self-assembly of the brush molecules into some ordered lamellar-like morphology (see, Fig. 17 on the right). These factors are most likely responsible for hampering the adsorption of the NPs at higher N_B.

The short-time dynamics of the LCNPs is examined via evaluation of the average mean square displacements (MSDs) of the core beads. Evaluation is performed by compiling the MSD profile along z, over time intervals Δt

$$MSD(\Delta t, z) = \langle [\mathbf{r}_i(t_2) - \mathbf{r}_i(t_1)]^2 \rangle |_{z_i(t_1)=z}, \quad t_2 - t_1 = \Delta t. \tag{19}$$

The averaging is performed over the core beads of all LCNPs and over all available initial time instances t_1 within the averaging intervals of adsorption runs, as defined above. The result is shown in Fig. 18 as a series of overlapping plots for an equidistant time intervals Δt for four cases of $N_B = 0, 4, 16$ and 36. This allows for monitoring the increase of MSD with Δt at each separation z from the bottom wall.

With no brush present, $N_B = 0$, the MSDs are arranged in stripes following the layering arrangement of LCNPs shown earlier in Fig. 16. At the same Δt, the height of each stripe is found to be approximately equal. The increase of MSD upon an increase of Δt in each z-bin is approximately linear for $\Delta > 0.24\,\text{ns}$ indicating the start of the diffusive regime. At higher brush density, $N_B = 4$, no changes in the LCNPs arrangement were seen in Fig. 16. However, the small number of brush molecules is able to immobilise the LCNPs within the brush region: $z < 0.25Lz \approx 14$. A similar effect is observed at $N_B = 16$ and 36, where the adsorbed LCNPs are found to be immobilised within the approximate height of the brush, $z < 0.4Lz \approx 22$ and $z < 0.5Lz \approx 27$, respectively. At the highest value of $N_B = 36$, the mobility of NPs in the bulk part of the box is seriously reduced, also. The reason can be seen in the increase in the local density of NPs there, due to their expulsion from the brush region.

To conclude this section, the coarse-grained model for the polymer brush and LC-NPs, where both components contain similar LC groups, predicts several outcomes. First, the optimal brush density exists, $N_B = 16$ for this particular model setup, that is characterized by the maximal adsorption of the LCNPs on the brush. It is a consequence of competition between two tendencies while the brush density increases. The first tendency is the enhancement of the LCNPs adsorption because of the larger number of the LC groups within the brush; whereas the second one is the decrease of adsorption because of a reduction of available free volume within a brush and enhanced self-assembly of the chain molecules themselves.

The brush density value $N_B \approx 16$ is also confirmed as the most optimal one for LCNPs adsorbtion by analyzing short-time dynamics of the NPs. In particular, despite the fact that at $N_B = 16$ and $N_B = 36$ the adsorbed LCNPs are located approximately at the top of the brush, for the latter case, the dynamics of LCNPs in the bulk part of the box is seriously reduced. The reason for this can be an increase of the local density of NPs there, due to their expulsion from the brush region.

8. Conclusions

We have reviewed our recent progress in the area of computer simulation studies of the aided and self-assembly behaviour of liquid crystalline nanoparticles (LCNPs). These complex systems are composed of nanoparticles, which are decorated and functionalised by mesogenic ligands. These materials have a range of fascinating behaviour linked to their self-assembly and self-organisation, including the subtle effects of shape change on bulk phase behaviour, and the interaction of these nanoparticles with other forms of soft matter including surfaces. These systems are immensely difficult to model. They are too computationally demanding to study at an atomistic simulation level and simple lattice models or continuum models are not able to capture the coupling between changes in molecular structure and the interactions of the particles with their surroundings. However, we have shown recently that the use of coarse-grained models composed of soft-core interactions provides a mechanism to simulate the complex behaviour arising in bulk phases composed of these particles.

In this paper, we show that these coarse-grained models are capable of capturing smectic and hexagonal discotic phases arising from situations where the nanoparticles adopt rod-like and disc-like morphologies. Moreover, we show how the density of ligands around a central nanoparticle is important in self-selecting these morphologies. Here we demonstrate also how coarse-grained modelling opens up the possibility of studying the effects on bulk phase interactions of LCP design choices, such as the use of lateral or terminally bonded mesogens. These coarse-grained models also open up the possibility of studying the effect of photo-aided self-assembly when appropriate chromophores are incorporated into the nanoparticle ligands. In these cases, photo-illumination can change ligand shape, which, in turn, changes the interaction of the LCP with its environment. We also show how macromolecular network formation can be controlled by selected functionalisation of the nanoparticle, generating nanoparticles with different shapes, which behave differently in terms of the morphologies of the macromolecular networks that these shapes induce.

We have also demonstrated how LCPs can interact with surfaces and polymer brushes. Here, the fascinating interplay between microphase separation, adsorption of the nanoparticles onto the surface of a brush and incorporation of the nanoparticles into the brush itself produces a rich compendium of behaviour, which can be tuned by LCP concentration and the density of ligands around the central nanoparticle core. Modelling provides a molecular-level picture of this complex behaviour.

Finally, we suggest that these models provide a powerful aid in the future design of new functional soft matter systems. Systems in which the effects of ligand density, ligand connectivity, temperature-mediated interactions, microphase separation and photo-induced and/or field-induced ordering can be both understood and utilized to engineer new effects.

Acknowledgements

AS, DY and JI are grateful to the Ukranian Army for protection during the work on this study.

References

[1] Yokoyama M, Hosokawa K, Nogi M, et al., editors. Nanoparticle technology handbook. Amsterdam: Elsevier; 2008.

[2] Hepel M, Zhong CJ, editors. Functional nanoparticles for bioanalysis, nanomedicine, and bioelectronic devices volume 1. American Chemical Society; 2012. Available from: http://dx.doi.org/10.1021/bk-2012-1112.

[3] Kumar SK, Ganesan V, Riggleman RA. Perspective: Outstanding theoretical questions in polymer-nanoparticle hybrids. J Chem Phys. 2017;147(2):020901. Available from: https://doi.org/10.1063/1.4990501.

[4] Ariga K, Nishikawa M, Mori T, et al. Self-assembly as a key player for materials nanoarchitectonics. Sci Technol Adv Mater. 2019;20(1):51–95. Available from: https://doi.org/10.1080/14686996.2018.1553108.

[5] Kumar S. Nanoparticles in discotic liquid crystals. In: Series in soft condensed matter. World Scientific; 2016. p. 461–496. Available from: https://doi.org/10.1142/9789814619264_0013.

[6] Draper M, Saez IM, Cowling SJ, et al. Self-assembly and shape morphology of liquid crystalline gold metamaterials. Adv Funct Mater. 2011;21(7):1260–1278. Available from: http://dx.doi.org/10.1002/adfm.201001606.

[7] Heinz H, Pramanik C, Heinz O, et al. Nanoparticle decoration with surfactants: Molecular interactions, assembly, and applications. Surf Sci Rep. 2017;72(1):1–58. Available from: https://doi.org/10.1016/j.surfrep.2017.02.001.

[8] Agrawal AK, Kumar K, Swarnakar NK, et al. "liquid crystalline nanoparticles": Rationally designed vehicle to improve stability and therapeutic efficacy of insulin following oral administration. Mol Pharmaceutics. 2017;14(6):1874–1882. Available from: https://doi.org/10.1021/acs.molpharmaceut.6b01099.

[9] Choudhary A, George T, Li G. Conjugation of nanomaterials and nematic liquid crystals for futuristic applications and biosensors. Biosensors. 2018;8(3):69. Available from: https://doi.org/10.3390/bios8030069.

[10] Shen Y, Dierking I. Perspectives in liquid-crystal-aided nanotechnology and nanoscience. Applied Sciences. 2019;9(12):2512. Available from: https://doi.org/10.3390/app9122512.

[11] Voth G, editor. Coarse-graining of condensed phase and biomolecular systems. CRC Press; 2008.

[12] Rühle V, Junghans C, Lukyanov A, et al. Versatile object-oriented toolkit for coarse-graining applications. J Chem Theory Comput. 2009;5(12):3211–3223. Available from: https://doi.org/10.1021/ct900369w.

[13] Orlandi S, Zannoni C. Phase organization of mesogen-decorated spherical nanoparticles. Mol Cryst Liq Cryst. 2013;573(1):1–9. Available from: https://doi.org/10.1080/15421406.2012.763213.

[14] Baran Ł, Sokołowski S. A comparison of molecular dynamics results for two models of nanoparticles with fixed and mobile ligands in two-dimensions. Appl Surf Sci. 2017; 396:1343–1351. Available from: https://doi.org/10.1016/j.apsusc.2016.11.159.

[15] Hughes ZE, Wilson MR, Stimson LM. Coarse-grained simulation studies of a liquid crystal dendrimer: towards computational predictions of nanoscale structure through microphase separation. Soft Matter. 2005;1(6):436. Available from: http://dx.doi.org/10.1039/B511082C.

[16] Ilnytskyi J, Lintuvuori J, Wilson MR. Simulation of bulk phases formed by polyphilic liquid crystal dendrimers. Condens Matter Phys. 2010;13(3):33001. Available from: http://dx.doi.org/10.5488/CMP.13.33001.

[17] Ponomarenko SA, Boiko NI, Shibaev VP, et al. Carbosilane liquid crystalline dendrimers: from molecular architecture to supramolecular nanostructures. Macromolecules. 2000; 33(15):5549–5558. Available from: https://doi.org/10.1021/ma0001032.

[18] Ponomarenko SA, Rebrov EA, Bobrovsky AY, et al. Liquid crystalline carbosilane dendrimers: First generation. Liq Cryst. 1996;21(1):1–12. Available from: https://doi.org/10.1080/02678299608033789.

[19] Lorenz K, Hölter D, Stühn B, et al. A mesogen-functionized carbosilane dendrimer: A dendritic liquid crystalline polymer. Adv Mat. 1996;8(5):414–416. Available from: https://onlinelibrary.wiley.com/doi/abs/10.1002/adma.19960080509.

[20] Lang H, L uhmann B. Siloxane and carbosiloxane based dendrimers: Synthesis, reaction chemistry, and potential applications. Adv Mat. 2001;13(20):1523–1540.

[21] Yonetake K, Masuko T, Morishita T, et al. Poly (propyleneimine) dendrimers peripherally modified with mesogens. Macromolecules. 1999;32(20):6578–6586.

[22] Barberá J, Marcos M, Serrano JL. Dendromesogens: liquid crystal organizations versus starburst structures. Chem –Eur J. 1999;5(6):1834–1840.

[23] Lintuvuori JS, Wilson MR. A new anisotropic soft-core model for the simulation of liquid crystal mesophases. J Chem Phys. 2008;128(4):044906. Available from: http://dx.doi.org/10.1063/1.2825292.

[24] Groot RD, Warren PB. Dissipative particle dynamics: Bridging the gap between atomistic and mesoscopic simulation. J Chem Phys. 1997;107(11):4423–4435. Available from: https://doi.org/10.1063/1.474784.

[25] Wilson MR. Molecular dynamics simulations of flexible liquid crystal molecules using a gay-berne/lennard-jones model. J Chem Phys. 1997;107(20):8654–8663. Available from: https://doi.org/10.1063/1.475017.

[26] Wilson MR, Ilnytskyi JM, Stimson LM. Computer simulations of a liquid crystalline dendrimer in liquid crystalline solvents. J Chem Phys. 2003;119(6):3509. Available from: http://dx.doi.org/10.1063/1.1588292.

[27] Ilnytskyi J, Wilson MR. A domain decomposition molecular dynamics program for the simulation of flexible molecules with an arbitrary topology of lennard–jones and/or gay–berne sites. Comput Phys Commun. 2001;134(1):23–32. Available from: https://doi.org/10.1016/s0010-4655(00)00187-9.

[28] Ilnytskyi JM, Wilson MR. A domain decomposition molecular dynamics program for the simulation of flexible molecules of spherically-symmetrical and nonspherical sites. II. extension to NVT and NPT ensembles. Comput Phys Commun. 2002;148(1):43–58. Available from: https://doi.org/10.1016/s0010-4655(02)00467-8.

[29] Ilnytskyi JM, Neher D. Structure and internal dynamics of a side chain liq-

uid crystalline polymer in various phases by molecular dynamics simulations: A step towards coarse graining. J Chem Phys. 2007;126(17):174905. Available from: http://dx.doi.org/10.1063/1.2712438.

[30] Ilnytskyi J. Relation between the grafting density of liquid crystal macromolecule and the symmetry of self-assembled bulk phase: coarse-grained molecular dynamics study. Condens Matter Phys. 2013;16(4):43004. Available from: http://dx.doi.org/10.5488/CMP.16.43004.

[31] Lewandowski W, Fruhnert M, Mieczkowski J, et al. Dynamically self-assembled silver nanoparticles as a thermally tunable metamaterial. Nature Comm. 2015;6(1):1–9.

[32] Saez IM, Goodby JW. Supermolecular liquid crystals. J Mater Chem. 2005;15(1):26. Available from: http://dx.doi.org/10.1039/b413416h.

[33] Saez IM, Goodby JW. Supermolecular liquid crystals. In: Liquid crystalline functional assemblies and their supramolecular structures. Springer Berlin Heidelberg; 2008. p. 1–62. Available from: https://doi.org/10.1007/430_2007_077.

[34] Bisoyi HK, Kumar S. Liquid-crystal nanoscience: an emerging avenue of soft self-assembly. Chem Soc Rev. 2011;40(1):306–319. Available from: https://doi.org/10.1039/b901793n.

[35] Agina EV, Boiko NI, Richardson RM, et al. Synthesis, structure, and phase behavior of carbosilane LC dendrimers with terminal butoxyphenylbenzoate mesogenic groups. Polym Sci Ser A+. 2007;49(4):412–424. Available from: https://doi.org/10.1134/s0965545x07040086.

[36] Wójcik M, Lewandowski W, Matraszek J, et al. Liquid-crystalline phases made of gold nanoparticles. Angew Chem Int Ed. 2009;48(28):5167–5169. Available from: http://dx.doi.org/10.1002/anie.200901206.

[37] Wojcik M, Kolpaczynska M, Pociecha D, et al. Multidimensional structures made by gold nanoparticles with shape-adaptive grafting layers. Soft Matter. 2010;6(21):5397. Available from: https://doi.org/10.1039/c0sm00539h.

[38] Wojcik MM, Gora M, Mieczkowski J, et al. Temperature-controlled liquid crystalline polymorphism of gold nanoparticles. Soft Matter. 2011;7(22):10561. Available from: https://doi.org/10.1039/c1sm06436c.

[39] Ilnytskyi JM, Saphiannikova M. Reorientation dynamics of chromophores in photosensitive polymers by means of coarse-grained modeling. ChemPhysChem. 2015;16(15):3180–3189. Available from: http://dx.doi.org/10.1002/cphc.201500500.

[40] Slyusarchuk A, Ilnytskyi J. Novel morphologies for laterally decorated metaparticles: molecular dynamics simulation. Condens Matter Phys. 2014;17(4):44001. Available from: http://dx.doi.org/10.5488/CMP.17.44001.

[41] Ikeda T, Mamiya J, Yu Y. Photomechanics of liquid-crystalline elastomers and other polymers. Angew Chem Int Ed. 2007;46(4):506–528. Available from: http://dx.doi.org/10.1002/anie.200602372.

[42] Wilson MR, Stimson LM, Ilnytskyi JM. The influence of lateral and terminal substitution on the structure of a liquid crystal dendrimer in nematic solution: A computer simulation study. Liq Cryst. 2006;33(10):1167–1175. Available from: https://doi.org/10.1080/02678290600973113.

[43] Ilnytskyi JM, Slyusarchuk A, Saphiannikova M. Photocontrollable self-assembly of azobenzene-decorated nanoparticles in bulk: Computer simulation study. Macromolecules. 2016;49(23):9272–9282. Available from: https://doi.org/10.1021/acs.macromol.6b01871.

[44] Klajn R, Stoddart JF, Grzybowski BA. Nanoparticles functionalised with reversible molecular and supramolecular switches. Chem Soc Rev. 2010;39(6):2203–2237.

[45] Bisby RH, Mead C, Morgan CG. Active uptake of drugs into photosensitive liposomes and rapid release on uv photolysis ¶. Photochem Photobiol. 2000;72(1):57–61.

[46] Liu X, Jiang M. Optical switching of self-assembly: Micellization and micelle–hollow-sphere transition of hydrogen-bonded polymers. Angew Chem Int Ed. 2006;118(23):3930–3934.

[47] Raimondo C, Crivillers N, Reinders F, et al. Optically switchable organic field-effect transistors based on photoresponsive gold nanoparticles blended with poly (3-hexylthiophene).

Proc Nat Acad Sci. 2012;109(31):12375–12380.

[48] Gallani JL, Hilliou L, Martinoty P, et al. Abnormal viscoelastic behavior of side-chain liquid-crystal polymers. Phys Rev Lett. 1994;72(13):2109–2112. Available from: http://dx.doi.org/10.1103/PhysRevLett.72.2109.

[49] Ilnytskyi JM, Neher D, Saphiannikova M. Opposite photo-induced deformations in azobenzene-containing polymers with different molecular architecture: Molecular dynamics study. J Chem Phys. 2011;135(4):044901. Available from: http://dx.doi.org/10.1063/1.3614499.

[50] Doi M, Edwards S. The theory of polymer dynamics. Oxford: Clarendon Press; 1994.

[51] van der Spoel D, van Maaren PJ, Berendsen HJC. A systematic study of water models for molecular simulation: Derivation of water models optimized for use with a reaction field. J Chem Phys. 1998;108(24):10220. Available from: http://dx.doi.org/10.1063/1.476482.

[52] Ikeda T. Photomodulation of liquid crystal orientations for photonic applications. J Mater Chem. 2003;13(9):2037. Available from: http://dx.doi.org/10.1039/b306216n.

[53] Ikeda T, Horiuchi S, Karanjit DB, et al. Photochemically induced isothermal phase transition in polymer liquid crystals with mesogenic phenyl benzoate side chains. 2. photochemically induced isothermal phase transition behaviors. Macromolecules. 1990;23(1):42–48. Available from: http://dx.doi.org/10.1021/ma00203a009.

[54] Barrett CJ, Mamiya J, Yager KG, et al. Photo-mechanical effects in azobenzene-containing soft materials. Soft Matter. 2007;3(10):1249. Available from: http://dx.doi.org/10.1039/B705619B.

[55] Petrova T, Toshchevikov V, Saphiannikova M. Light-induced deformation of polymer networks containing azobenzene chromophores and liquid crystalline mesogens. Soft Matter. 2015;11(17):3412–3423. Available from: http://dx.doi.org/10.1039/C5SM00019J.

[56] Todorov T, Nikolova L, Tomova N. Polarization holography 1: A new high-efficiency organic material with reversible photoinduced birefringence. Appl Opt. 1984;23(23):4309. Available from: http://dx.doi.org/10.1364/AO.23.004309.

[57] Michl J, Thulstrup EW, editors. Spectroscopy with polarized light: Solute alignment by photoselection, liquid crystal, polymers, and membranes corrected software edition. VCH Publishers; 1995. Available from: http://eu.wiley.com/WileyCDA/WileyTitle/productCd-0471186244.html.

[58] Hostetler MJ, Templeton AC, Murray RW. Dynamics of place-exchange reactions on monolayer-protected gold cluster molecules. Langmuir. 1999;15(11):3782–3789. Available from: https://doi.org/10.1021/la981598f.

[59] Freund HJ, Libuda J, Bäumer M, et al. Cluster, facets, and edges: Site-dependent selective chemistry on model catalysts. The Chemical Record. 2003;3(3):181–201. Available from: https://doi.org/10.1002/tcr.10060.

[60] Sperling RA, Parak WJ. Surface modification, functionalization and bioconjugation of colloidal inorganic nanoparticles. Philos Trans Royal Soc A. 2010;368(1915):1333–1383. Available from: https://doi.org/10.1098/rsta.2009.0273.

[61] Pawar AB, Kretzschmar I. Fabrication, assembly, and application of patchy particles. Macromol Rapid Commun. 2010;:NA–NAAvailable from: https://doi.org/10.1002/marc.200900614.

[62] Dias CS, Araújo NAM, da Gama MMT. Non-equilibrium adsorption of 2anb patchy colloids on substrates. Soft Matter. 2013;9(23):5616. Available from: https://doi.org/10.1039/c3sm50386k.

[63] Choueiri RM, Galati E, Thérien-Aubin H, et al. Surface patterning of nanoparticles with polymer patches. Nature. 2016;538(7623):79–83. Available from: https://doi.org/10.1038/nature19089.

[64] Kumar S, Pal SK, Lakshminarayanan V. Discotic-decorated gold nanoparticles. Mol Cryst Liq Cryst. 2005;434(1):251/[579]–258/[586]. Available from: https://doi.org/10.1080/15421400590956261.

[65] Sergeyev S, Pisula W, Geerts YH. Discotic liquid crystals: a new generation of organic semiconductors. Chem Soc Rev. 2007;36(12):1902. Available from:

https://doi.org/10.1039/b417320c.

[66] Kumar S. Discotic liquid crystal-nanoparticle hybrid systems. NPG Asia Materials. 2014; 6(1):e82–e82. Available from: https://doi.org/10.1038/am.2013.75.

[67] Ilnytskyi JM, Slyusarchuk A, Sokołowski S. Gelation of patchy ligand shell nanoparticles decorated by liquid-crystalline ligands: computer simulation study. Soft Matter. 2018; 14(19):3799–3810. Available from: https://doi.org/10.1039/c8sm00356d.

[68] Baran Ł, Sokołowski S. Effective interactions between a pair of particles modified with tethered chains. J Chem Phys. 2017;147(4):044903. Available from: https://doi.org/10.1063/1.4994919.

[69] Gröschel AH, Walther A, Löbling TI, et al. Guided hierarchical co-assembly of soft patchy nanoparticles. Nature. 2013;503(7475):247–251. Available from: https://doi.org/10.1038/nature12610.

[70] Fowler PW, Quinn CM, Redmond DB. Decorated fullerenes and model structures for water clusters. J Chem Phys. 1991;95(10):7678–7681. Available from: https://doi.org/10.1063/1.461341.

[71] Vukićević R, Beuermann S. Fullerenes decorated with poly(vinylidene fluoride). Macromolecules. 2011;44(8):2597–2603. Available from: https://doi.org/10.1021/ma102754c.

[72] Estrada E. Metric and topological structure of networks. In: The structure of complex networks. Oxford University Press; 2011. p. 47–71.

[73] Fogelholm R. The conductivity of large percolation network samples. J Phys C: Solid State Phys. 1980;13(23):L571–L574. Available from: https://doi.org/10.1088/0022-3719/13/23/001.

[74] Nandivada H, Ross AM, Lahann J. Stimuli-responsive monolayers for biotechnology. Prog Polym Sci. 2010;35(1-2):141–154. Available from: https://linkinghub.elsevier.com/retrieve/pii/S0079670009001075.

[75] Hou L, Wang L, Zhang N, et al. Polymer brushes on metal–organic frameworks by UV-induced photopolymerization. Polym Chem. 2016;7(37):5828–5834. Available from: http://xlink.rsc.org/?DOI=C6PY01008C.

[76] Feng C, Huang X. Polymer Brushes: Efficient Synthesis and Applications. Acc Chem Res. 2018;51(9):2314–2323. Available from: https://pubs.acs.org/doi/10.1021/acs.accounts.8b00307.

[77] Cheng S, Stevens MJ, Grest GS. Ordering nanoparticles with polymer brushes. J Chem Phys. 2017;147(22):224901. Available from: https://doi.org/10.1063/1.5006048.

[78] Santer S, Rühe J. Motion of nano-objects on polymer brushes. Polymer. 2004;45(25):8279–8297. Available from: https://doi.org/10.1016/j.polymer.2004.09.085.

[79] Loebner S, Jelken J, Yadavalli N, et al. Motion of adsorbed nano-particles on azobenzene containing polymer films. Molecules. 2016;21(12):1663. Available from: https://doi.org/10.3390/molecules21121663.

[80] Kumar S, Dory YL, Lepage M, et al. Surface-grafted stimuli-responsive block copolymer brushes for the thermo-, photo- and pH-sensitive release of dye molecules. Macromolecules. 2011;44(18):7385–7393. Available from: https://doi.org/10.1021/ma2010102.

[81] Nie G, Li G, Wang L, et al. Nanocomposites of polymer brush and inorganic nanoparticles: preparation, characterization and application. Polym Chem. 2016;7(4):753–769. Available from: https://doi.org/10.1039/c5py01333j.

[82] Uekusa T, Nagano S, Seki T. Unique molecular orientation in a smectic liquid crystalline polymer film attained by surface-initiated graft polymerization. Langmuir. 2007; 23(8):4642–4645. Available from: https://doi.org/10.1021/la063467h.

[83] Lysyakova L, Lomadze N, Neher D, et al. Light-tunable plasmonic nanoarchitectures using gold nanoparticle–azobenzene-containing cationic surfactant complexes. The Journal of Physical Chemistry C. 2015;119(7):3762–3770. Available from: https://doi.org/10.1021/jp511232g.

[84] Kopyshev A, Galvin CJ, Patil RR, et al. Light-induced reversible change of roughness and thickness of photosensitive polymer brushes. ACS Applied Materials & Interfaces. 2016;8(29):19175–19184. Available from: https://doi.org/10.1021/acsami.6b06881.

[85] Santer S. Remote control of soft nano-objects by light using azobenzene containing surfactants. J Phys D: Appl Phys. 2017;51(1):013002. Available from: https://doi.org/10.1088/1361-6463/aa95ca.

[86] Jelken J, Santer S. Light induced reversible structuring of photosensitive polymer films. RSC Advances. 2019;9(35):20295–20305. Available from: https://doi.org/10.1039/c9ra02571e.

[87] Slyusarchuk AY, Yaremchuk DL, Ilnytskyi JM. Adsorption of decorated nanoparticles on a liquid crystalline polymer brush: molecular dynamics study. Mathematical Modeling and Computing. 2020;7(2):207–218. Available from: https://doi.org/10.23939/mmc2020.02.207.

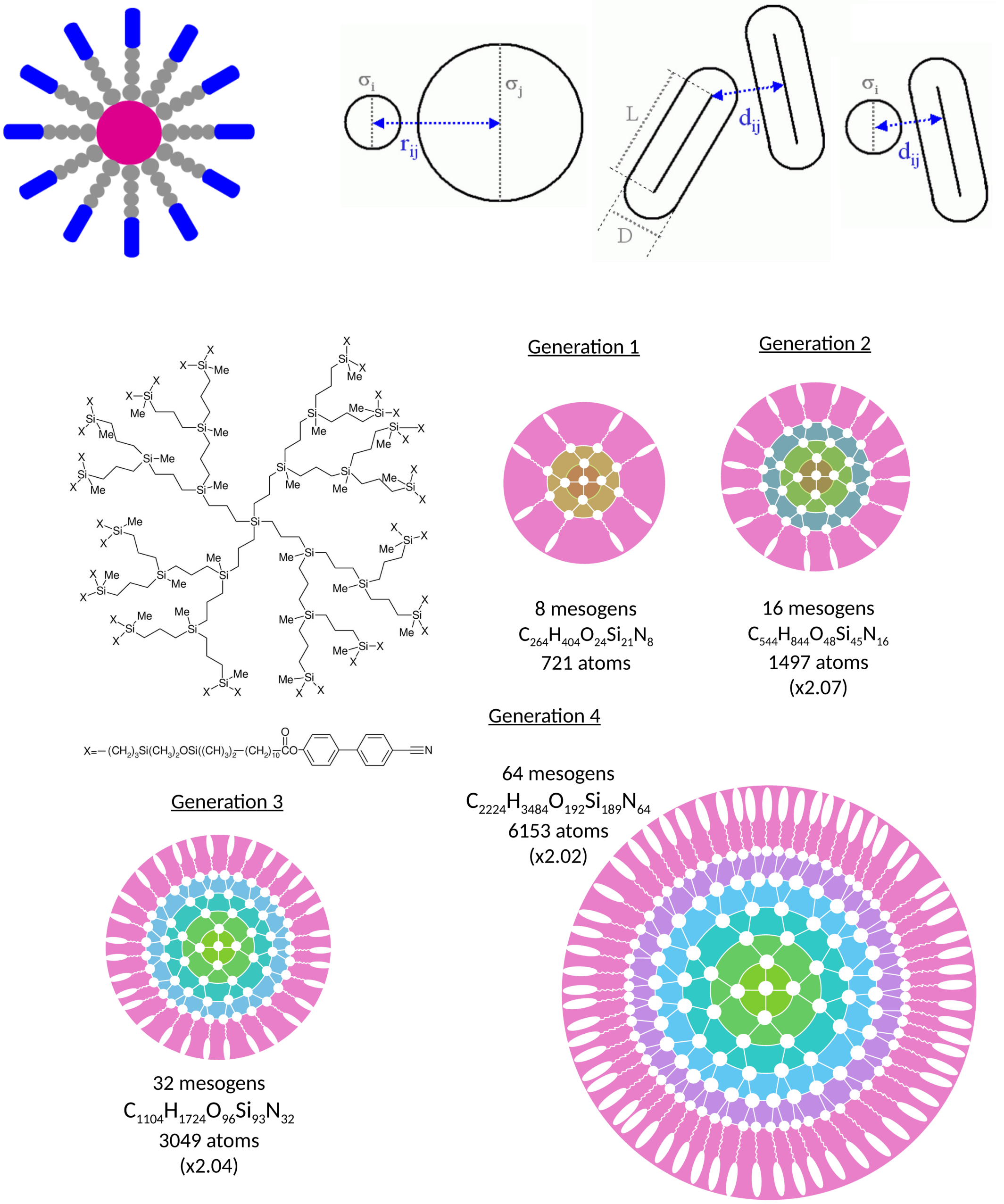

Figure 1. Top left frame: schematic representation of a model LCNP with 12 ligands (spherical core is depicted in pink, polymer spacers are shown as a chain of gray spheres, mesogens are shown as blue spherocylinders). Top frame: definition of particles' dimensions and pair distances. Middle left frame: chemical structure of a third generation carbosilane liquid crystalline dendrimer [17]. Middle right frame and bottom frames: schematic diagrams showing the branching points and liquid crystalline groups of 1st, 2nd, 3rd and 4th generation carbosilane liquid crystalline dendrimers.

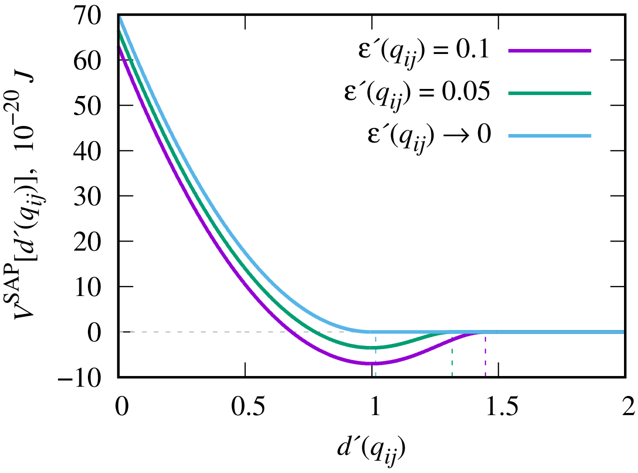

Figure 2. Illustration of the interaction potential $V^{\mathrm{SAP}}[d'(\mathbf{q}_{ij})]$ between two beads of any type shown for a range of effective dimensionless well depths $\epsilon'(\mathbf{q}_{ij})$ (respective cutoffs d'_c are indicated via vertical dashed lines). $d'(\mathbf{q}_{ij})$ is the minimum distance between the beads cores, which reduces to the dimensionless separation r'_{ij} between the centers for the case of two interacting spherical beads. At the well depth approaching zero, $\epsilon'(\mathbf{q}_{ij}) \to 0$, the potential $V^{\mathrm{SAP}}[d'(\mathbf{q}_{ij})]$ turns into a purely repulsive potential $V^{\mathrm{SRP}}[d'(\mathbf{q}_{ij})]$, Eq. (3), see blue curve in the plot.

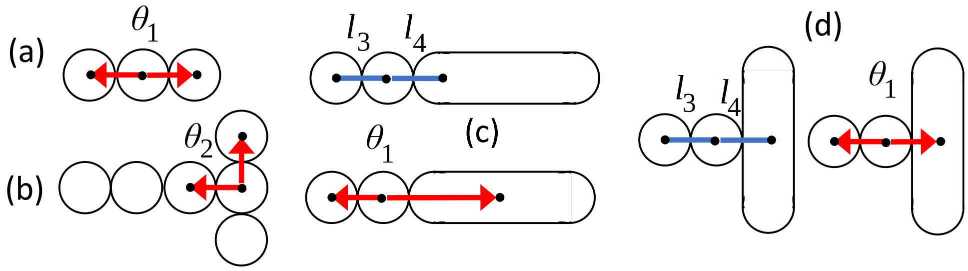

Figure 3. (a) Pseudovalent angle for linear polymeric fragments; (b) the same at branching point; (c) bonds (in blue) and pseudovalent angles for terminal attachment of mesogens; (d) the same for lateral attachment of mesogens. Parameters l_3, l_4, θ_1 and θ_2 are provided in Tab. 1.

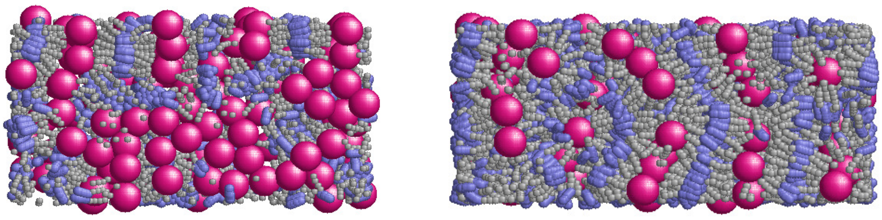

Figure 4. Snapshots illustrating self-assembly of LCNPs with $N_{\mathrm{ch}} = 8$ (left frame) and $N_{\mathrm{ch}} = 48$ (right frame) ligands when the melt at the temperature $T = 500K$ is cooled down to $450K$ with the rate of $25K/$ ns.

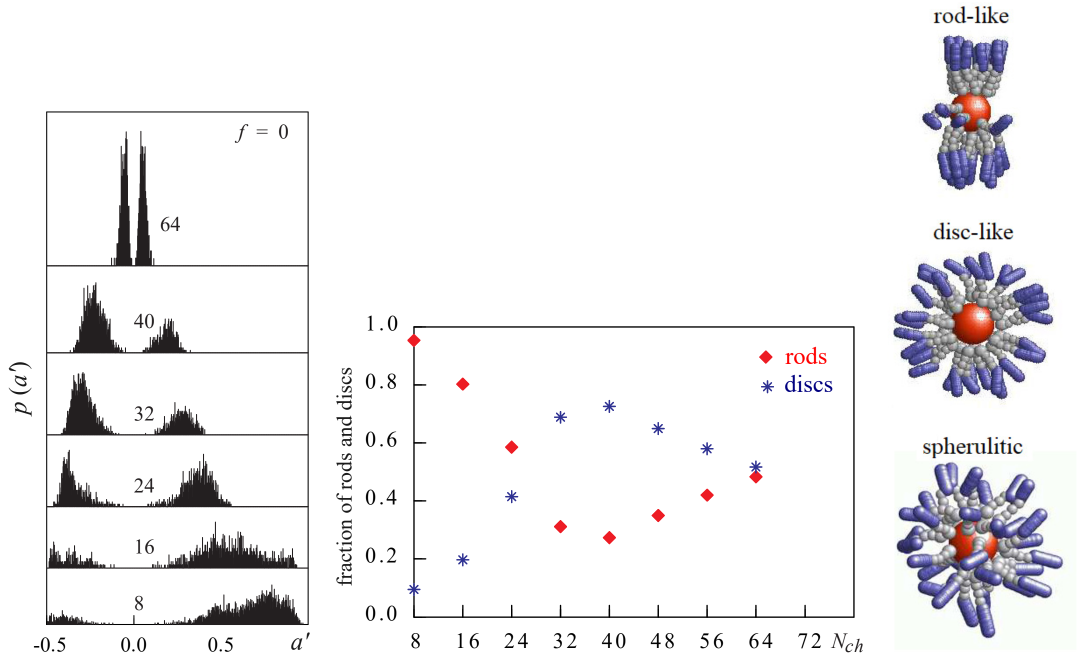

Figure 5. Histograms for the distributions of molecular asphericity $p(a')$ of LCNPs at various N_{ch}, as indicated next to each histogram in the figure (left frame), and the fractions f_r (diamonds) and f_d (asterisks) of rods and discs, respectively (middle frame). Typical molecular conformations at $N_{\text{ch}} = 32$ are displayed in the right frame. The case of spontaneous self-assembly of LCNP is shown here.

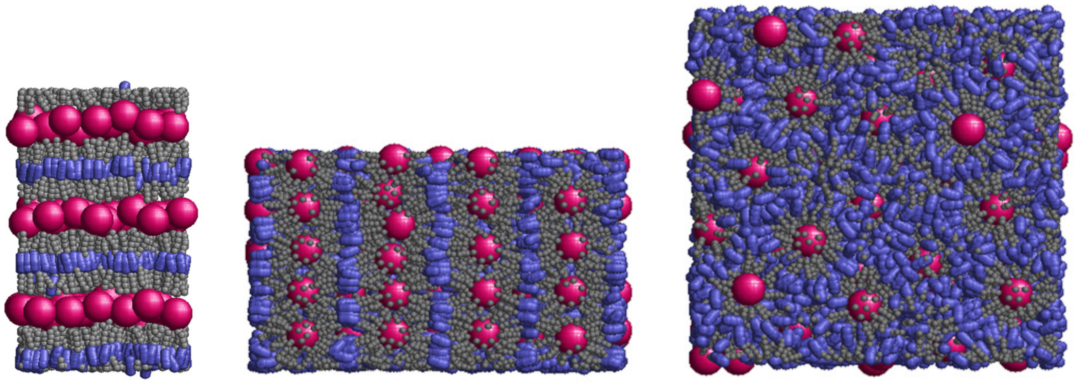

Figure 6. Snapshots illustrating field-aided self-assembly of LCNPs at $T = 450K$: lamellar morphology formed by LCNPs with $N_{\text{ch}} = 8$ ligands under uniaxial field (left frame), and columnar phase of LCNP with $N_{\text{ch}} = 48$ ligands under planar field (middle frame). The high temperature cubic phase at $T = 600K$ for LCNPs with $N_{\text{ch}} = 48$ is shown in the right frame.

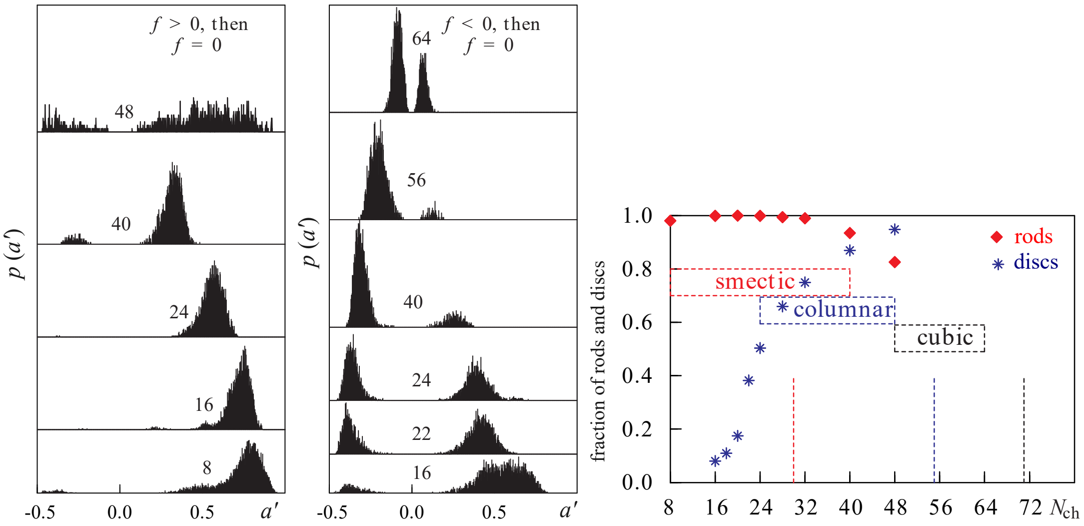

Figure 7. The same as in Fig. 4 for the case of aided assembly of LCNPs by uniaxial (marked $f > 0$ in the left and middle frames and diamonds in the right frame) and planar ($f < 0$ and asterisks) fields. The approximate phase boundaries for the smectic, columnar and cubic phases are also shown (dashed coloured horizontal text boxes), as well as the optimal numbers for space-filling of rod, disc and sphere from geometry estimates (vertical red, blue and black dashed lines, respectively).

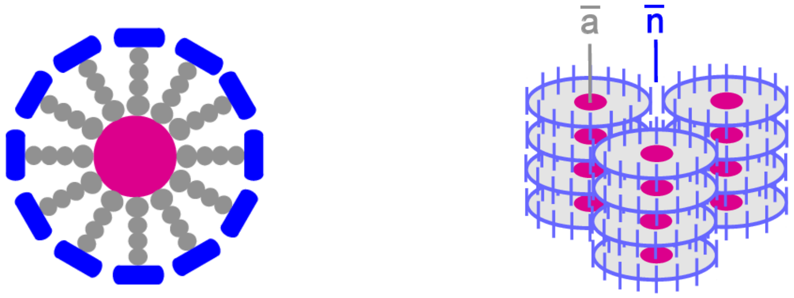

Figure 8. LCNP with lateral attachment of mesogens (left frame) and uniaxial Col morphology (right frame).

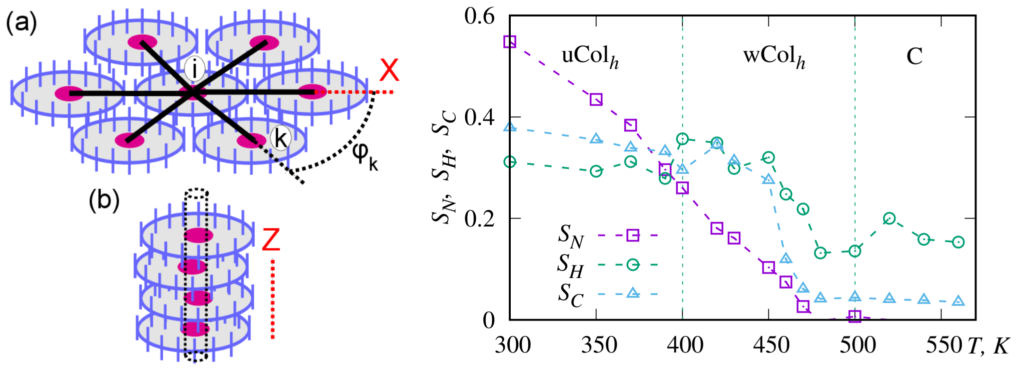

Figure 9. (a) Flat hexagonal cluster of LCNPs and the definition of bond angles φ_k. (b) A column of stacked LCNPs. Order parameters S_N, S_H and S_C upon heating the uCol$_h$ are shown in the rightmost frame.

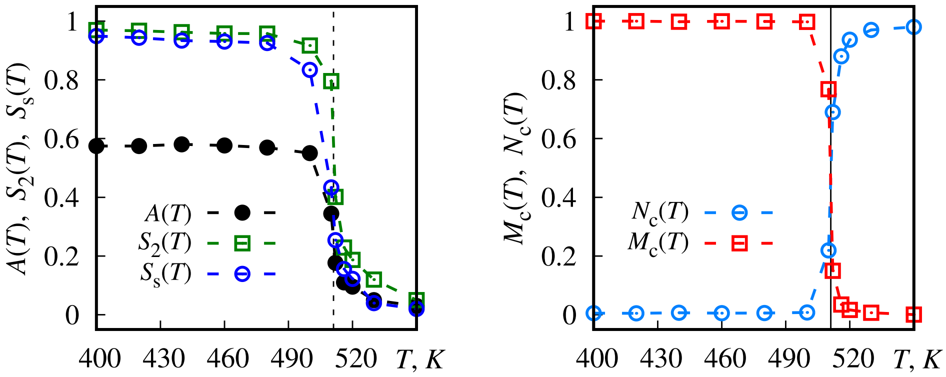

Figure 10. Molecular asphericity A, nematic S_2 and smectic S_s order parameters, reduced number of clusters N_c and normalized maximum cluster size M_c obtained when the monodomain $\mathrm{Sm_A}$ phase was heated at each indicated temperature. Each symbol represents result of a separate run. Reprinted with permission from J.M. Ilnytskyi, A. Slyusarchuk and M. Saphiannikova, Macromolecules, 49, pp. 9272–9282, 2016. © 2016 American Chemical Society.

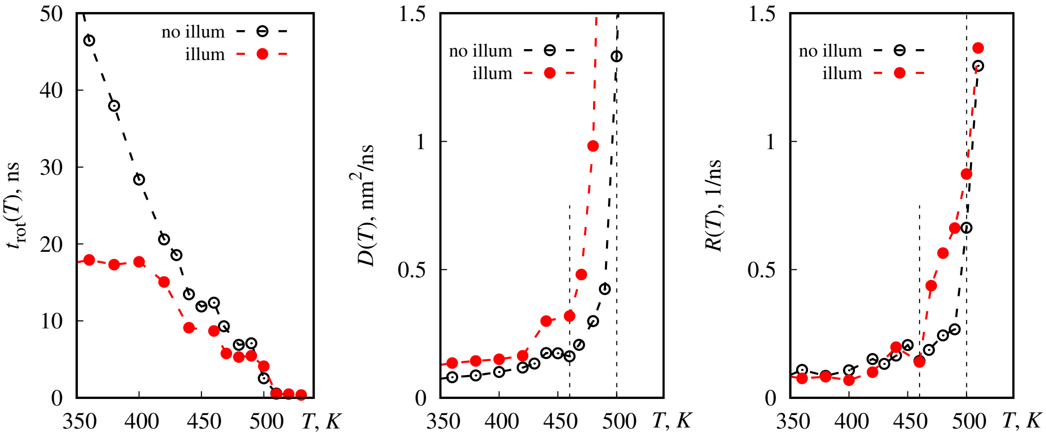

Figure 11. Chromophores rotation relaxation time t_{rot} and short-time translational D and rotational R diffusion coefficients. Reprinted with permission from J.M. Ilnytskyi, A. Slyusarchuk and M. Saphiannikova, Macromolecules, 49, pp. 9272–9282, 2016. © 2016 American Chemical Society.

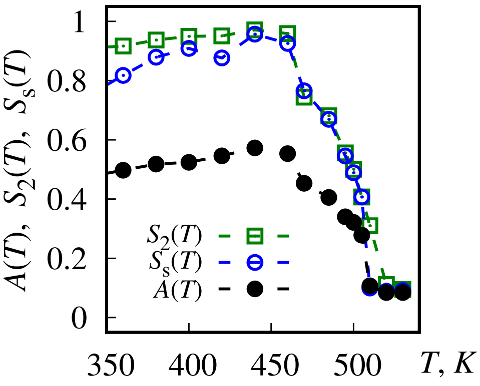

Figure 12. Molecular asphericity A, nematic S_2 and smectic S_s order parameters, reduced number of clusters N_c and normalized maximum cluster size M_c obtained when the isotropic phase was cooled down at each indicated temperature. Each symbol represents result of a separate run. Reprinted with permission from J.M. Ilnytskyi, A. Slyusarchuk and M. Saphiannikova, Macromolecules, 49, pp. 9272–9282, 2016. © 2016 American Chemical Society.

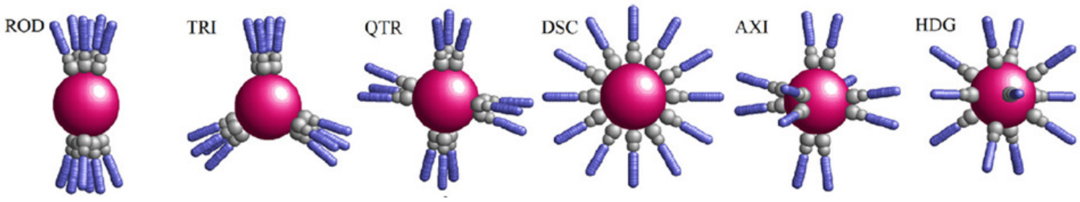

Figure 13. A set of the model LCNPs with predefined decoration patterns. The pattern as a whole, is free to move on a surface of the core, but mutual positions of patchy bunches are kept constant by imposing intra- and interpatch bonds and angles. Reproduced from Ref. [67] with permission from the Royal Society of Chemistry.

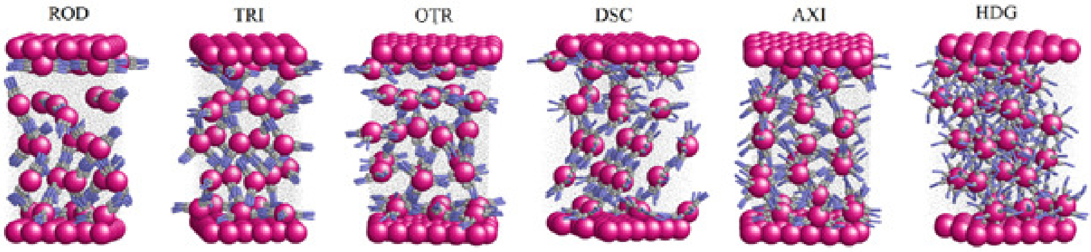

Figure 14. Snapshots illustrating typical LCNP network structures. These are obtained for each type of the decoration pattern as introduced in Fig. 13 for the case of $N_{\mathrm{mol}} = 27$. Reproduced from Ref. [67] with permission from the Royal Society of Chemistry.

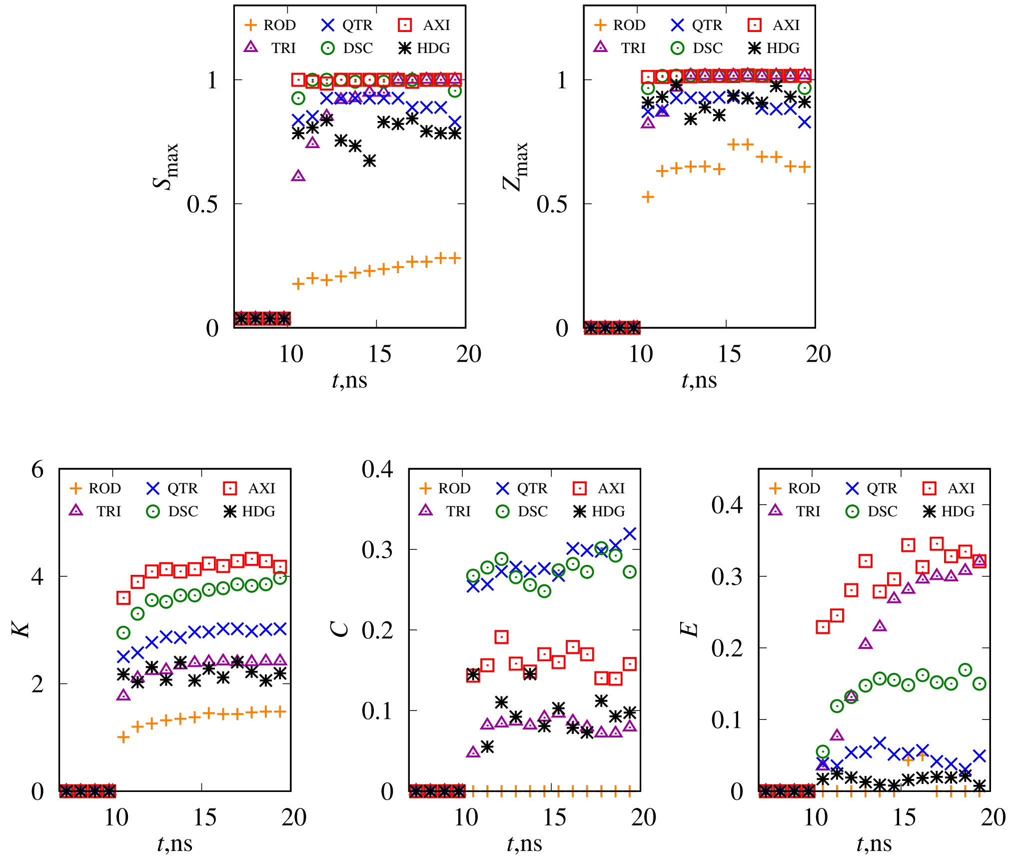

Figure 15. Time evolution for the largest cluster size $S_{\max}$, its span along OZ axis $Z_{\max}$, average vertex range K of the network, its average local clastering coefficient C and effective wall-to-wall spring constant E for different decoration patterns according to their nomenclature in Fig. 13. The case of $N_{\mathrm{mol}} = 27$ LCNP molecules is shown. Reproduced from Ref. [67] with permission from the Royal Society of Chemistry.

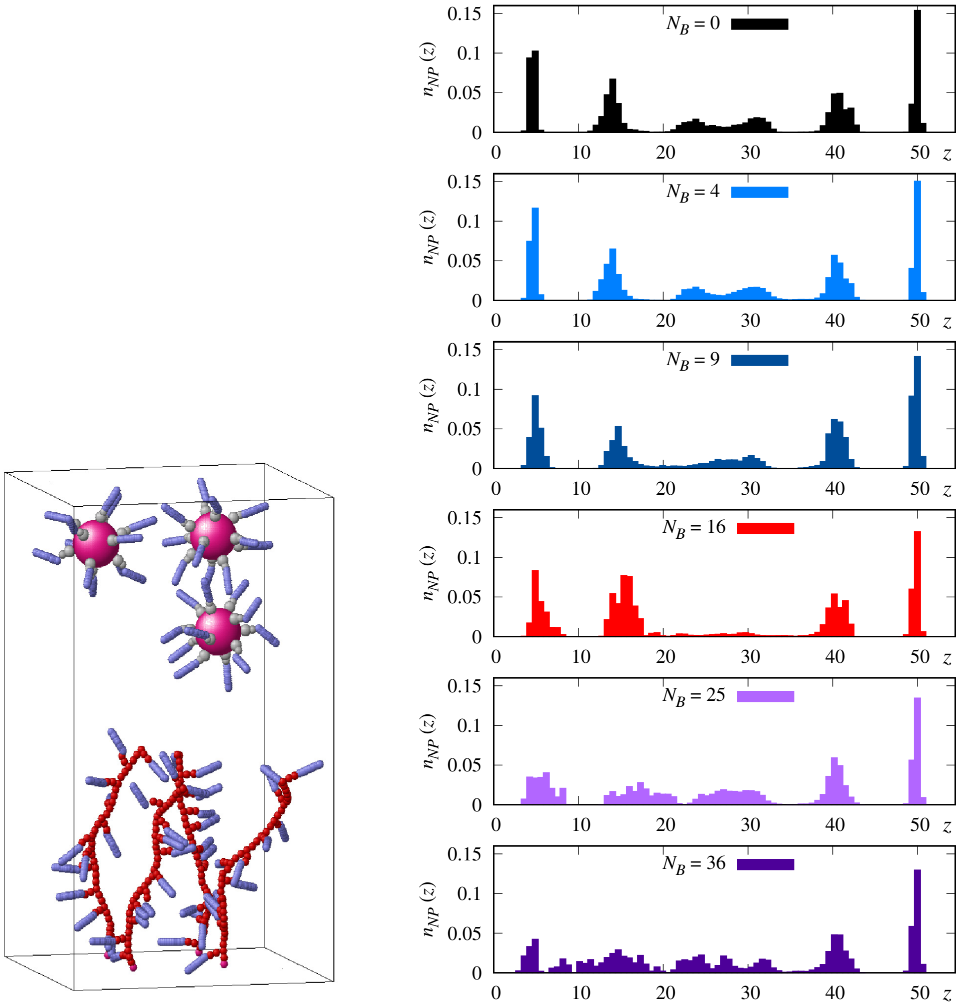

Figure 16. Left frame: Illustration for a model setup of LC brush and LCNPs. Right frame: histograms for the normalized number density profiles $n_{NP}(z)$ for the LCNP cores along the Z-axis at various number N_B of brush molecules (indicated in each plot).

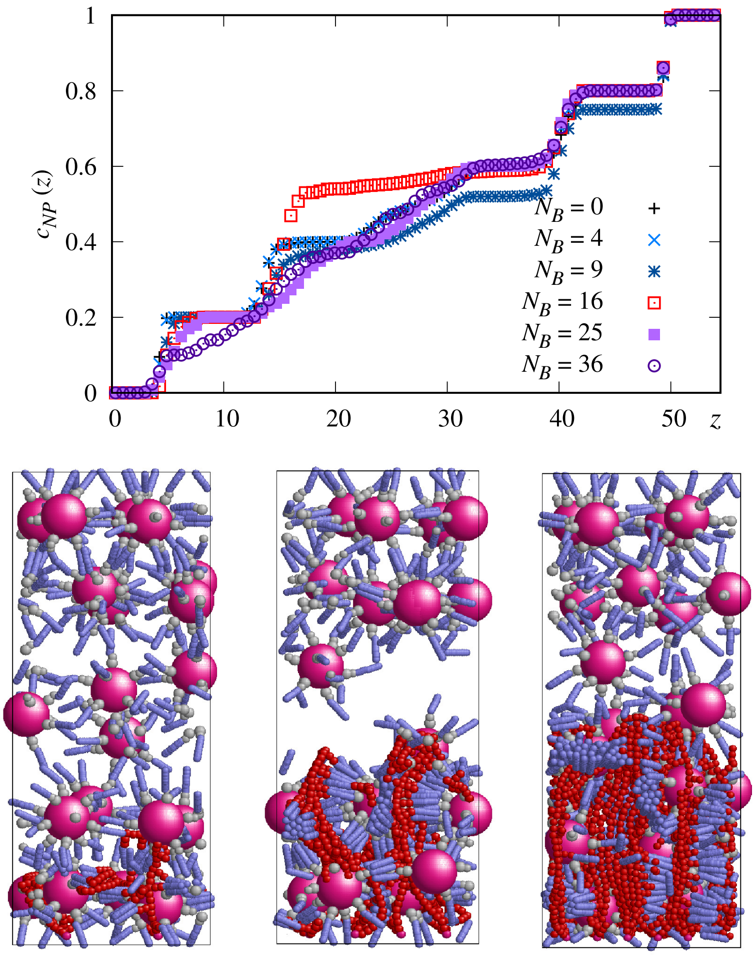

Figure 17. Top frame: cumulative number density $c_{\mathrm{NP}}(z)$ for the LCNP cores along the Z-axis at various number N_B of brush molecules (indicated in each plot). Bottom frames: snapshots for the brush and the LCNPs system at number of brush molecules N_B, from left to right: $N_B = 4$, $N_B = 16$ and $N_B = 36$.

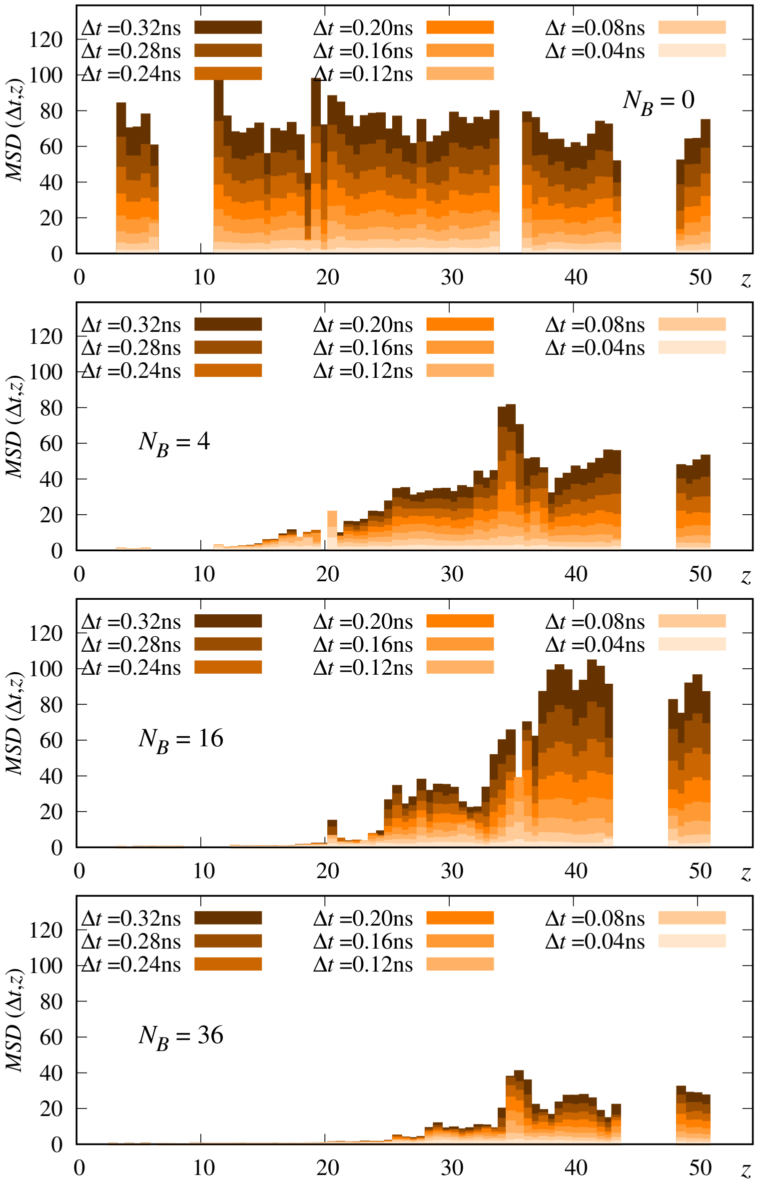

Figure 18. The average mean square displacements $MSD(\Delta t, z)$ of the core beads at equidistant time intervals Δt binned along the Z-axis. The number N_B of brush molecules is indicated in each plot.